

# EXTRAPLANAR EMISSION-LINE GAS IN EDGE-ON SPIRAL GALAXIES. II. OPTICAL SPECTROSCOPY

SCOTT T. MILLER<sup>1,2</sup> AND SYLVAIN VEILLEUX<sup>1,3,4</sup>

Department of Astronomy, University of Maryland, College Park, MD 20742;

stm, veilleux@astro.umd.edu

Draft version October 29, 2018

## ABSTRACT

The results from deep long-slit spectroscopy of nine edge-on spiral galaxies with known extraplanar line emission are reported. Emission from  $H\alpha$ ,  $[N\ II]\lambda\lambda 6548, 6583$ , and  $[S\ II]\lambda\lambda 6716, 6731$  is detected out to heights of a few kpc in all of these galaxies. Several other fainter diagnostic lines such as  $[O\ I]\lambda 6300$ ,  $[O\ III]\lambda\lambda 4959, 5007$ , and  $He\ I\lambda 5876$  are also detected over a smaller scale. The relative strengths, centroids and widths of the various emission lines provide constraints on the electron density, temperature, reddening, source(s) of ionization, and kinematics of the extraplanar gas. In all but one galaxy, photoionization by massive OB stars alone has difficulties explaining all of the line ratios in the extraplanar gas. Hybrid models that combine photoionization by OB stars and another source of ionization such as photoionization by turbulent mixing layers or shocks provide a better fit to the data. The (upper limits on the) velocity gradients measured in these galaxies are consistent with the predictions of the galactic fountain model to within the accuracy of the measurements.

*Subject headings:* diffuse radiation – galaxies: halos – galaxies: ISM – galaxies: spiral – galaxies: structure

## 1. INTRODUCTION

Emission-line diagnostics have been used successfully to determine the hardness of the ionizing spectrum in Galactic and extragalactic H II regions (e.g., Stasinska 1982; Evans & Dopita 1985; McCall, Rybski, & Shields 1985; Dopita et al. 2000 and references therein) and in the nuclei of galaxies (e.g., Baldwin, Phillips, & Terlevich 1981; Veilleux & Osterbrock 1987; Osterbrock, Tran, & Veilleux 1992; Veilleux 2002 and references therein), but only over the last decade has it been possible to measure the emission line ratios in the faint, extraplanar diffuse ionized gas (eDIG) of external galaxies (e.g., reviews by Dettmar 1992 and Dahlem 1997). Observations of the diffuse ionized gas in our own Galaxy show line ratios which are difficult to explain with pure stellar photoionization models without extra heating (e.g., Reynolds 1985a, 1985b; Reynolds & Tufte 1995; Mathis 2000). A similar situation appears to apply to external galaxies. The  $[N\ II]\lambda 6583/H\alpha$  and  $[S\ II]\lambda 6716, 6731/H\alpha$  line ratios measured in a few galaxies generally become stronger with increasing heights, often reaching values considerably higher than typical values observed in H II regions (e.g., Rand, Kulkarni, & Hester 1990; Keppel et al. 1991; Dettmar & Schultz 1992; Veilleux, Cecil, & Bland-Hawthorn 1995; Ferguson, Wyse, & Freeman 1996; Golla, Dettmar, & Domgörgen, 1996; Domgörgen & Dettmar 1997; Rand 1998; Otte & Dettmar 1999; Tüllman & Dettmar 2000; Tüllman et al. 2000; Miller & Veilleux 2003a, hereafter Paper I). The vertical  $[N\ II]/H\alpha$  and  $[S\ II]/H\alpha$  gradients detected in these galaxies may be due to hardening of the OB-star radiation as it passes through the dusty and neutral medium of the galaxy, or to the existence of other sources of heating or ionization which is becoming increasingly important above the galactic plane. Possible sources of extra ionization and heating include shocks, photoionization by cooling hot gas, “turbulent mixing layers”

(TML; Slavin, Shull, & Begelman 1993) or supernova remnants (Slavin, McKee, & Hollenbach 2000), cosmic ray heating (e.g., Lerche & Schlickeiser 1982; Hartquist & Morfill 1986; Parker 1992), and magnetic reconnection (e.g., Raymond 1992).

The measurements of additional line ratios can shed some light on the importance of secondary ionization sources. One particularly important line ratio is  $[O\ III]\lambda 5007/H\alpha$ , a good indicator of high energy processes. However,  $[O\ III]$  is challengingly faint and has therefore been measured in only a few galaxies (e.g., Rand 1998; Tüllman & Dettmar 2000; Tüllman et al. 2000; Collins & Rand 2001). This is also the case for  $He\ I\lambda 5876/H\alpha$ , a sensitive indicator of the hardness of the ionizing radiation. Interestingly, the value of  $He\ I/H\alpha$  in NGC 891, a galaxy which in many ways is very similar to our own, appears significantly larger than the Galactic value ( $0.034$  versus  $0.012 \pm 0.006$ ; Reynolds & Tufte 1995; Rand 1997), while the value observed in NGC 3044 is even larger ( $\sim 0.07$ ; Tüllman & Dettmar 2000).  $[O\ II]\lambda 3727/H\beta$  has recently been shown to be a useful diagnostic of extra heating in the diffuse ionized gas (Mathis 2000; Otte et al. 2001; Otte, Gallagher, & Reynolds 2002), but  $H\beta$  emission is generally very faint outside of H II regions and  $[O\ II]\lambda 3727/H\alpha$  is highly sensitive to reddening corrections and flux calibration errors.

There is a need to expand the set of high-quality spectroscopic observations of the eDIG to a larger number of galaxies. This paper describes an attempt to remedy this situation. The results from a spectroscopic survey of nine edge-on galaxies with known eDIG are reported. Due to scheduling constraints, the imaging observations reported in Paper I were not reduced and analyzed in time for our scheduled spectroscopic observations, so the spectroscopic sample was selected independently of the imaging sample. The only exception is NGC 2820, where the  $H\alpha$  image obtained with the TTF (see Paper I) was used to

<sup>1</sup> Visiting Astronomer, Kitt Peak National Observatory and Cerro Tololo Inter-American Observatory, National Optical Astronomy Observatory, which is operated by the Association of Universities for Research in Astronomy, Inc. (AURA) under cooperative agreement with the National Science Foundation

<sup>2</sup> Current address: Department of Astronomy, Pennsylvania State University, 525 Davey Lab., University Park, PA 16802; stm@astro.psu.edu

<sup>3</sup> Current address: 320-47 Downs Lab., Caltech, Pasadena, CA 91125 and Observatories of the Carnegie Institution of Washington, 813 Santa Barbara Street, Pasadena, CA 91101; veilleux@ulirg.caltech.edu

<sup>4</sup> Cottrell Scholar of the Research Corporation

determine the optimum slit position [note that NGC 4013 is also in the imaging sample of Paper I, but the position of the slit for this object is based on earlier observations by Rand (1996; hereafter R96)]. The nine galaxies in the spectroscopic sample were selected based on the published reports of extraplanar emission by Pildis, Bregman, & Schombert (1994b, hereafter PBS) and R96. The methods used to acquire and reduce these data are discussed in §2. Great care is taken to reach a limiting surface brightness of order a few  $10^{-18}$  erg s $^{-1}$  cm $^{-2}$  arcsec $^{-2}$ . The results from the spectroscopic analysis are given in §3. New constraints on the physical conditions in the eDIG (e.g., temperature, density, reddening, ionization level, kinematics) are derived using the relative strengths and positions of the stronger emission lines that lie within 4550 – 7300 Å. In §4, the line ratios derived from the long-slit spectra are compared with values measured in other galaxies, as well as with predictions from photoionization models (Sokolowski 1994; Bland-Hawthorn et al. 1997), turbulent mixing layer models (Slavin et al. 1993), and shock models (Shull & McKee 1979; Dopita & Sutherland 1995). This analysis allows us to determine whether a secondary source of ionization in addition to photoionization by hot stars is needed in the eDIG. The main results are summarized in §5.

## 2. DATA ACQUISITION AND REDUCTION

All of the data were taken at the KPNO 2.1-m telescope on January 22 – 26, 1998. A compromise had to be made between broad wavelength coverage and good spectral resolution. Grating #26new and filter GG-420 were used with the F3KA CCD to provide a dispersion of 1.256 Å pixel $^{-1}$  and a useful spectral coverage of  $\sim 2760$  Å between  $\sim 4550$  and 7300 Å, after accounting for the known bad columns on the redward side of the F3KA CCD. The slit width was set at 1''/5, yielding a spectral resolution of  $\sim 3.7$  Å. This configuration allows us to resolve the H $\alpha$  + [N II]  $\lambda\lambda 6548, 6583$  complex, the [S II]  $\lambda\lambda 6717, 6731$  doublet, and the He I  $\lambda 5876$  line from the nearby Na ID sky lines, but does not cover the important [O II]  $\lambda 3727$  and [O III]  $\lambda 4363$  diagnostic lines. The length of the slit in this mode is 5''/2, extending well beyond the extent of the galaxy disks in our sample. The CCD was binned in the spatial direction by a factor of 2 in order to increase the signal per pixel from the diffuse emission, resulting in a spatial scale of 1''/56 pixel $^{-1}$ . To reach our goal of achieving a flux limit on the order of a few  $\times 10^{-18}$  erg s $^{-1}$  cm $^{-2}$  arcsec $^{-2}$ , each galaxy was observed for about 5 hours. Details on the observations are listed in Table 2. The slit was centered on the disk of the galaxy and in most cases positioned so that it lay perpendicular to the disk, although in a few cases it was tilted slightly to optimize the coverage of the extraplanar emission. The position of the slit is mentioned in Table 2 and shown in Figure 1 for each galaxy in the sample. All galaxies were observed through an airmass of less than  $\sim 1.5$  to avoid any significant differential atmospheric refraction.

Bias frames were taken each night and a composite bias was made by combining the individual frames. The bias level was found not to be constant across the CCD, showing a gradient along the dispersion axis. A one-dimensional fit was applied along the dispersion axis to create the bias frame, making sure not to introduce additional noise to the data when subtracting off the bias. The spectra were then trimmed and corrected for bias and overscan using the CCDPROC package in IRAF. Both dome and internal (quartz) flats were obtained during the night with the purpose to use them for the flatfield and illumination

corrections. However, better results were obtained when using the domeflats to flatfield the data, and the data themselves to correct for the illumination along the slit. For this procedure, each spectrum was binned along the dispersion axis so that each wavelength bin was well represented and contained sufficient counts. The illumination variations across the slit were accurately modeled using the IRAF ILLUMINATION routine to fit a spline function to the background while avoiding the emission due to the galaxy.

Next the data were corrected for distortion and wavelength calibrated using HeNeAr spectra. Observations of the HeNeAr lamp were obtained before and/or after each galaxy observation so that accurate corrections could be obtained. A fit to the sky background was calculated and subtracted from each frame using sample rows on either side of the galaxy, far enough from it to avoid the extraplanar emission. The two-dimensional spectra were then flux calibrated using HZ 44 as a calibrator and combined together.

After combining the different observations for each galaxy, the redshifted emission lines were identified based on the systemic optical velocity of each galaxy (as listed in de Vaucouleurs et al. 1991). The spatial dimension was further binned by two in order to increase the signal per binned pixel in the weaker lines, and one-dimensional spectra were extracted at different heights from the disk plane. The spatial dimension was binned even further at large  $|z|$  to help detect very faint extended line emission. The spectra for each galaxy are shown in Figure 2 as a function of position along the slit. In the case where a spectral line is not detected, a representative spectrum from near the disk plane is presented. The line fluxes were determined using the SPLIT routine in IRAF. Single gaussian profiles were fitted to each line in order to calculate the line flux and width and the level of the underlying continuum emission.

## 3. RESULTS

### 3.1. Line Ratios

The vertical profiles of up to nine diagnostic line ratios are shown in Figure 3 for each galaxy. In each figure, the vertical profile of the H $\alpha$  emission is shown as the heavy solid line and the continuum emission is shown as the dotted line. Both have been scaled arbitrarily for display purposes. To prevent the figures from becoming overcrowded, the error bars in all of the figures represent  $1\sigma$  uncertainties as determined from SPLIT. In most galaxies, H $\alpha$ , [N II]  $\lambda 6583$ , and [S II]  $\lambda\lambda 6716, 6731$  have been detected along the slit out to 1 – 2 kpc from the center of the disk (in most of our galaxies, the slit is perpendicular to the disk and this represents the actual vertical extent of the gas, but in a few cases this distance differs slightly from the vertical height; see Fig. 1). Fainter lines such as H $\beta$ , [O III]  $\lambda 4959, 5007$ , and He I  $\lambda 5876$  are also detected over a smaller scale in a number of galaxies. This section of the paper discusses the overall trends found in the sample. For a more detailed discussion of each object, the reader should refer to the Appendix.

#### 3.1.1. [N II]/H $\alpha$ , [S II]/H $\alpha$ , and [N II]/[S II]

The average midplane values for [N II]  $\lambda 6583$ /H $\alpha$  and [S II]  $\lambda 6716$ /H $\alpha$  are  $0.40 \pm 0.20$  and  $0.24 \pm 0.14$ , respectively. Seven galaxies show a general increase in [N II]/H $\alpha$  and [S II]/H $\alpha$  with increasing height. The most dramatic gradients occur within NGC 4013 and NGC 4217, where the [N II]/H $\alpha$  ratios are H II region-like in the disk ( $\sim 0.3 - 0.4$ ) but reach values of nearly 2.0 at  $|z| \sim 1 - 2$  kpc above the disk. Some of

the galaxies in the sample have [S II]  $\lambda 6716$ /[N II]  $\lambda 6583$  ratios which change with height; some (such as NGC 2820 and UGC 4278) show a steady increase with increasing  $|z|$ . Others (such as NGC 4302) show a general decrease with increasing height. Most interesting is NGC 4217, which shows an increase in [S II]/[N II] from 0.5 to 0.7 up to  $|z| \sim 1$  kpc, and then the ratio falls to 0.3 at higher  $|z|$ . Other galaxies present [S II]/[N II] ratios which are consistent with being constant within the uncertainties of the measurements.

For comparison, Rand (1998) found in NGC 891 that the [N II]/H $\alpha$  line ratio rises from 0.35 in the plane of this galaxy, to a value greater than unity at  $|z| \sim 2 - 3$  kpc. A similar trend was found with the [S II]/H $\alpha$  line ratio, such that the [S II]/[N II] ratio remained almost constant with a value  $\sim 0.6$ . Observations of a few other galaxies (Collins & Rand 2001; Tüllmann & Dettmar 2000) find similar trends. The ratio of collisionally excited lines (like [N II] and [S II]) to recombination lines (like H $\alpha$ ) depends on the ratio of heating to recombination. Since S<sup>0</sup> and N<sup>0</sup> have similar ionization potentials (10.4 eV and 14.5 eV, respectively), any changes in the [S II]/[N II] ratio suggest changes in the local ionization condition (S<sup>+</sup> ionizes at a slightly lower ionization energy than N<sup>+</sup>), or in the metallicity (since nitrogen is a secondary product of nucleosynthesis while sulphur is a primary product). These issues are discussed further in §4.2 and §4.3 below.

### 3.1.2. He I/H $\alpha$

He I  $\lambda 5876$  is detected in the disk of only 4 of the 9 sample galaxies (the presence of the Na ID absorption lines in at least 4 of the galaxies makes detection of this line impossible - see Fig. 2 for details). Emission from H II regions in the disks of the galaxies is almost certainly contaminating some of these measurements. The midplane value of He I/H $\alpha$  for these galaxies ranges from 0.018 (NGC 4013) to 0.052 (NGC 4302), bracketing the value measured in Orion (0.042; Kaler 1976) but larger than the value measured in the diffuse ionized gas near the midplane of our Galaxy ( $0.012 \pm 0.006$ ; Reynolds & Tufté 1995). The relative ionization fractions of helium and hydrogen can be determined by the equation:

$$\frac{E_{5876}}{E_{H\alpha}} = 0.048 \frac{\chi_{He}}{\chi_H} \left( \frac{He/H}{0.1} \right) \left( \frac{T}{8000 \text{ K}} \right)^{-0.14} \quad (1)$$

(e.g., Brockelhurst 1971; Martin 1988; Reynolds & Tufté 1995; Rand 1997), where  $E$  is the emissivity in  $\text{cm}^{-3} \text{ s}^{-1}$ ,  $\chi$  is the fraction of helium or hydrogen that is singly ionized, He/H is the abundance of helium with respect to hydrogen by number, and  $T$  is the gas temperature. Using the He/H abundance listed in Boesgaard & Steigman (1995) and  $T = 8000$  K (e.g., Reynolds 1992),  $\chi_{He}/\chi_H$  is found to range from 0.38 to 1.09. If hydrogen is assumed to be mostly ionized (a reasonable assumption given the strength of [O III] in the eDIG of several galaxies; see §4.2), then the helium is about 40% ionized in NGC 4013, and is almost fully ionized in NGC 4302. Using Table 1 of Rand (1997),  $Q_{He}/Q_H$ , the ratio of He-ionizing ( $h\nu > 24.6$  eV) to H-ionizing ( $h\nu > 13.6$  eV) photons, ranges from  $\sim 0.040$  to 0.115. These results imply an effective temperature of the radiation field,  $T_*$ , which ranges from about 36,500 to 38,500 K, and an upper limit to the stellar mass function,  $M_*$ , which ranges from  $\sim 42$  to  $54 M_\odot$ .

Extraplanar He I emission is detected unambiguously in only one galaxy of our sample, NGC 2820. This object has a midplane He I/H $\alpha$  value of 0.046, and a range of values from 0.033

to 0.056 (the latter at a height of  $|z| = 1$  kpc). Corresponding values of [N II]/H $\alpha$  are  $\sim 0.25$  at the midplane, and range from 0.16 to  $\sim 0.3$  at  $|z| = 1$  kpc. Within the uncertainties, these values are consistent with the predictions from the O-star photoionization models of Domgörgen & Mathis (1994). Rand (1997) had difficulties reconciling the values of He I/H $\alpha$  with those of [N II]/H $\alpha$  in NGC 891, but the extraplanar [N II]/H $\alpha$  line ratios in this galaxy are much higher (near 1.4). Extraplanar He I was not detected in any of the galaxies of our sample with large extraplanar [N II]/H $\alpha$  ratios.

### 3.1.3. Reddening from H $\alpha$ /H $\beta$

The H $\alpha$ /H $\beta$  line ratio is shown in the bottom left panel of Figure 3 for each galaxy (when detected). No correction was made for possible underlying stellar absorption features; these features were never evident in the data. This line ratio provides an indication of the amount of reddening affecting the spectra. Determining the amount of reddening is not straightforward, however. Typical H $\alpha$ /H $\beta$  line ratios for H II regions is  $\sim 2.85$ , but if shocks are present, this ratio could rise to  $\sim 3.10$  (e.g., Shull & McKee 1979). The effects of extinction and reddening also depend on the distribution of the dust with respect to the source of emission (e.g., uniform screen in front of the source of emission *versus* uniform dust distribution mixed with the line emitting gas). Rather than to try to correct for these complex effects, we instead list in Table 3 the impact on the line ratios of a foreground screen of dust with  $A_V = 1$ . Except for H $\alpha$ /H $\beta$  and [O III]/H $\alpha$ , the line ratios shown in Figure 3 are not at all sensitive to reddening.

In general the amount of reddening is found to be larger in the disk than in the eDIG, as one would expect if the dust is distributed near the plan of the galaxy disk. Out of the five galaxies in which extraplanar H $\beta$  was detected, three clearly show this trend. In the other two galaxies, the H $\alpha$ /H $\beta$  line ratio appears to be relatively constant with height (NGC 2820) or does not show any obvious monotonic trend with height (NGC 4013).

### 3.1.4. Density from [S II] $\lambda 6716$ /[S II] $\lambda 6731$

The [S II]  $\lambda 6716$ /[S II]  $\lambda 6731$  ratio is shown in the bottom middle frame of Figure 3 for each galaxy (when detected). The ratio of the intensities of these lines yield information on the average electron density of the gas. The low density limit of this line ratio is  $\sim 1.4$ , and so it is possible to make quantitative statements regarding the density of the gas only in regions where this line ratio is less than  $\sim 1.4$ .

For most of the galaxies, the [S II]  $\lambda 6716$ /[S II]  $\lambda 6731$  line ratio is consistent with the low density limit, therefore suggesting an electron density of at most a few tens of  $\text{cm}^{-3}$ . This is typical of the electron density that has been reported for other galaxies (e.g., Rand 1998; Collins & Rand 2001). There are three exceptions: NGC 3628, NGC 4217, and NGC 4302. The results on NGC 3628 are discussed in the Appendix. In NGC 4217, the [S II]  $\lambda 6716$ /[S II]  $\lambda 6731$  line ratio has a value of  $\sim 1.2$  near the disk of the galaxy, and drops slightly to an average value of 0.9 at a height of about 1 kpc, before climbing back up over 1.4. Assuming a constant temperature of  $\sim 10^4$  K for the moment, this suggests that the electron density in the disk of the galaxy is  $\sim 200 \text{ cm}^{-3}$  and increases to a value of  $900 \text{ cm}^{-3}$  at heights  $\sim 1$  kpc, before decreasing below the low density limit. In NGC 4302, the value of the [S II]  $\lambda 6716$ /[S II]  $\lambda 6731$  line ratio near the disk of the galaxy is  $\sim 1.0$ , and decreases to values near 0.8 and 0.6 at heights of  $\sim 0.5$  kpc. The

corresponding electron densities are  $\sim 500 \text{ cm}^{-3}$  in the disk of the galaxy and 1000 to  $2000 \text{ cm}^{-3}$  at larger heights. It should be noted, however, that the electron density as measured by the [S II] ratio scales as  $T^{1/2}$  (e.g., Osterbrock 1989), and therefore an increase in temperature would be interpreted as higher electron density if constant temperature were assumed. The vertical temperature profiles in the eDIG of these galaxies are discussed next.

### 3.1.5. Temperature from $[N \text{ II}]/H\alpha$

Two of the best temperature gauges for the extraplanar gas are the  $[N \text{ II}] \lambda 6583/[N \text{ II}] \lambda 5755$  and  $[O \text{ III}] \lambda 5007/[O \text{ III}] \lambda 4363$  line ratios.  $[N \text{ II}] \lambda 5755$  was recently detected in the diffuse ionized gas of our Galaxy and indicates elevated temperatures relative to those of H II regions (Reynolds et al. 2001). Unfortunately the  $[N \text{ II}] \lambda 5755$  line was not detected in any of the sample galaxies and  $[O \text{ III}] \lambda 4363$  falls outside the wavelength range of our observations. We therefore have no choice but to use other line ratios for this analysis. Recent studies have suggested the use of the  $[N \text{ II}]/H\alpha$  line ratio as a temperature diagnostic (Haffner, Reynolds, & Tufte 1999), keeping in mind that the derived temperature is an average value over the line-of-sight column density. Given that hydrogen and nitrogen have similar first ionization potentials and a weak charge-exchange reaction, and assuming that hardly any N is doubly ionized, one has  $N^+/N^0 \approx H^+/H^0$ . Under this assumption and using a Galactic gas-phase abundance of  $(N/H) = 7.5 \times 10^{-5}$  at all heights (Meyer, Cardelli, & Sofia 1997), the relationship between the  $[N \text{ II}]/H\alpha$  line ratio and electron temperature is given by

$$\frac{[N \text{ II}]}{H\alpha} = 12.2 T_4^{0.426} e^{-2.18/T_4} \quad (2)$$

where  $T_4$  is the electron temperature in units of  $10^4 \text{ K}$  (Collins & Rand 2001). The detection of significant  $[O \text{ III}]$  emission in the eDIG of four galaxies of our sample ( $[O \text{ III}]/H\alpha \gtrsim 0.25$ ; UGC 4278, NGC 2820, NGC 4302 and NGC 5777) is inconsistent with the  $[N \text{ II}]/H\alpha$  temperature model (eqn. 2) because this model assumes that  $N^{++}$  is not present in the eDIG, yet the ionization potential of  $N^+$  (29.6 eV) is close to that of  $O^+$  (35.1 eV). Temperature profiles for the remaining five galaxies in the sample have been calculated using eqn. (2) and the measured  $[N \text{ II}]/H\alpha$  line ratios; the results are shown in the bottom, left panel of Figure 4 (the other panels will be discussed in §4.2). Three of these galaxies (NGC 3628, NGC 4013 and NGC 4217) show an increase in temperature with vertical distance from the disk. The change in temperature with height varies from galaxy to galaxy, with some objects showing no change with height within the uncertainties (e.g., UGC 2092 and UGC 3326), while others show a dramatic increase (e.g., NGC 4217: from 6000 K to almost 10,000 K). Haffner et al. (1999) detect an increase in electron temperature for our Galaxy from 7000 K at  $|z| = 0.75 \text{ kpc}$  to over 10,000 K at  $|z| = 1.75 \text{ kpc}$ . Collins & Rand (2001) find similar temperature gradients in their studies of edge-on galaxies.

### 3.2. Kinematics

The kinematics of the extraplanar gas can also provide insights into its nature and origin. To our knowledge, only two galaxies (NGC 891 and NGC 5775) have so far been examined with sufficient care to address this important issue. In both cases, the velocity of the extraplanar material is seen to approach the systemic velocity of the galaxy (Pildis, Bregman,

& Schommer 1994a; Rand 1997, 2000; Tüllman et al. 2000). This vertical velocity gradient can be explained by a combination of radial movement of the gas (following the pressure gradient of the halo) and declining rotation speed (conserving angular momentum), as predicted by the galactic fountain model (e.g., Bregman 1980; Houck & Bregman 1990).

Although our spectroscopic setup was chosen to optimize wavelength coverage at the expense of spectral resolution to allow us to carry out a detailed line ratio analysis of our objects, an attempt is made to constrain the kinematics of the eDIG in the galaxies of our sample. Figure 5 displays the velocity profiles for  $H\alpha$ ,  $[N \text{ II}] \lambda 6583$ , and  $[S \text{ II}] \lambda 6716$ , the strongest lines in our galaxies. These velocity profiles are not expected to differ significantly from each other, so comparisons between the three panels can serve to estimate the uncertainties of the velocity measurements. Galactic rotation causes a velocity offset from systemic in the cases where the slit does not pass through the nucleus. Figure 5 shows that most galaxies do not show significant vertical gradients within the accuracy of the measurements ( $\sim 30 - 50 \text{ km s}^{-1}$  depending on the galaxy). However, there appears to be a few exceptions. A significant dip in velocity ( $\delta v \approx 100 \text{ km s}^{-1}$ ) is observed at  $z \approx -0.3 \text{ kpc}$  in NGC 3628, coincident with the prominent dust lane in this object. Dust obscuration is severely limiting the use of the optical emission lines as kinematic probes in this region. Possibly significant gradients are also visible in NGC 2820 and NGC 4013 (and perhaps in NGC 4302 but at a lower significance level). In NGC 2820, the velocities reach a maximum of  $\sim 150 \text{ km s}^{-1}$  around  $z = +0.4 \text{ kpc}$  and then show a monotonic decrease toward systemic velocity at large heights, reaching values of  $\sim 80 \text{ km s}^{-1}$  at  $z \approx \pm 1.5 \text{ kpc}$ . A slightly less significant gradient of  $\sim 50 \text{ km s}^{-1}$  appears to be present on both sides of the disk of NGC 4013 out to  $|z| \approx 1 \text{ kpc}$ . The gradients observed in both of these galaxies can be explained if the rotational velocity of line-emitting material is lower above and below the galaxy disk, as expected in the galaxy fountain model. The amplitudes of the detected gradients are however larger than the predictions from the model of Bregman (1980). The ballistic model of Collins, Benjamin, & Rand (2002) has more success explaining the gradients in NGC 2820 and NGC 4013. The lack of obvious gradients in the other galaxies is not inconsistent with the predictions of the galactic fountain model of Bregman (1980), given the relatively large uncertainties in the measurements.

The widths of the emission lines provides another constraint on the gas kinematics. The lower right panels of Figure 5 show the line widths of  $H\alpha$ , selected because it is generally the strongest emission line in our galaxies. Typical values lie between  $\sim 100$  and  $200 \text{ km s}^{-1}$ . There is little or no evidence for significant line width gradients in the majority of the galaxies in our sample. The only galaxies where gradients may be present are NGC 3628 (coincident with the dust lane), UGC 3326 (the line widths vary from  $\sim 275 \text{ km s}^{-1}$  in the midplane to  $\sim 150 \text{ km s}^{-1}$  at heights near  $|z| = 1 \text{ kpc}$ ), NGC 4013 (a slight positive gradient of  $\sim 50 \text{ km s}^{-1}$  over  $\pm 0.5 \text{ kpc}$  on both sides of the disk may be present), and NGC 2820 (the line widths in this object are constant over most of the slit, but show a significant decrease from  $170 \text{ km s}^{-1}$  at  $|z| \sim 1 \text{ kpc}$  to  $\sim 80 \text{ km s}^{-1}$  at  $|z| \sim 1.7 \text{ kpc}$  in the southern halo of the galaxy). Numerical broadening arising from Poisson noise, whereby noisier signals tend to pull in more emission in the wings than at the peak, may affect (increase) the line widths at large  $|z|$ . Positive vertical line width gradients may also be due to increasingly turbulent mo-

tions at large heights (e.g., turbulent mixing layer; §4.3.1), or due to the fact that extinction by the disk is less significant at large heights (§3.1.3) and therefore a longer column of material with a broader range of velocities is being sampled. Our data do not allow us to distinguish between these various possibilities.

#### 4. DISCUSSION

Several models have been proposed to explain the line ratios detected in the extraplanar material of disk galaxies. In this section we discuss each of these models and compare their predictions with our data.

##### 4.1. Photoionization by OB Stars

OB stars are almost certainly contributing to the ionization of the eDIG. They are by far the main source of Lyman continuum flux produced in the disk (e.g., Reynolds 1984), but their position near the disk midplane makes them highly vulnerable to absorption by the ISM and dust. Photoionization models (e.g., Mathis 1986; Domgörgen & Mathis 1994; Sokolowski 1994; Bland-Hawthorn et al. 1997; Mathis 2000) have had some success explaining the increase in the [N II]/H $\alpha$  line ratio observed in the eDIG. This increase is attributed to a decrease with height of the ionization parameter ( $U$ ), a measure of the ratio of the ionizing photon number density ( $\Phi$ ) to the electron density ( $n_e$ ). Under the assumption of ionization equilibrium,  $\Phi \propto n_e^2$  at all heights. Therefore,  $U \propto \Phi/n_e \propto n_e$ , so the ionization parameter should fall off exponentially with height. As  $U$  decreases, lower ionization species are favored, leading to an increase in the [N II]/H $\alpha$  and [S II]/H $\alpha$  ratios and a decrease in the [O III]/H $\alpha$  ratio (neglecting the effects of reddening).

However, some problems arise with the photoionization models. First, pure stellar continua models have difficulty reproducing [N II]/H $\alpha$  and [S II]/H $\alpha$  ratios greater than unity, as detected in some of the galaxies of our sample and in other studies (e.g., Dettmar & Schultz 1992; Veilleux et al. 1995; Rand 1998; Collins & Rand 2001; Paper I). Photoionization models that take into account the multi-phase nature of the ISM, the possible depletion of certain gas-phase abundance of metals onto dust grains, and the absorption and hardening of the stellar radiation field as it propagates through the dust and H I gas in the disk (Sokolowski 1994; Bland-Hawthorn et al. 1997) are more successful at producing elevated [N II]/H $\alpha$  ratios of  $\sim 1.5$ . Unfortunately, these models have difficulties explaining the observed behavior of [O I] and [O III] relative to H $\alpha$ . Collins & Rand (2001) detect [O III] in three out of four of their galaxies, and observe in each one a general *increase* in the [O III]/H $\alpha$  line ratio with increasing height. Out of the five galaxies in which we detect [O III], three of them (NGC 2820, NGC 4302, and NGC 5777) show the same positive trend with height. A sharp increase in the [O I]/H $\alpha$  line, which is difficult to explain using photoionization models, is also observed in two galaxies of our sample (NGC 2820 and NGC 4217; see also Collins & Rand 2001; Rand 1998). A secondary source of heating and/or ionization appears to be needed to explain these observations.

##### 4.2. Secondary Source of Nonionizing Heating

We first explore the possibility of a nonionizing source of heating in the eDIG (e.g., photoelectric heating from dust grains, dissipation of interstellar turbulence). The apparent temperature gradients found in three galaxies in the sample (§3.1.5) bring support to this scenario but do not prove it. For this, one needs to also examine the behavior of the other line

ratios. Using the assumptions mentioned in §3.1.5 when deriving equation (2), Galactic gas-phase abundances of S, N, and O, and the fact that the ionization fractions of oxygen and hydrogen are coupled through a charge exchange reaction, Collins and Rand (2001; also Haffner et al. 1999) derive the following equations for the line ratio intensities as a function of temperature and ionization fraction:

$$\frac{[S II]}{H\alpha} = 14.3 \left[ \frac{S^+/S}{H^+/H} \right] T_4^{0.307} e^{-2.14/T_4}, \quad (3)$$

$$\frac{[S II]}{[N II]} = 1.2 \left[ \frac{S^+/S}{H^+/H} \right] T_4^{-0.119} e^{0.04/T_4}, \quad (4)$$

$$\frac{[O III]}{H\alpha} = 40 \left[ \frac{O^{++}/O}{H^+/H} \right] T_4^{0.52} e^{-2.87/T_4}, \quad (5)$$

$$\frac{[O I]}{H\alpha} = 7.9 \left[ \frac{1-(H^+/H)}{(H^+/H)} \right] \left[ \frac{T_4^{1.85}}{1+0.605T_4^{1.105}} \right] e^{-2.284/T_4}. \quad (6)$$

These equations implicitly assume that the metallicity of the eDIG is constant with height. Note that eqn. (4) predicts only a very weak temperature dependence for the [S II]/[N II] ratio. Using the temperature gradients derived in §3.1.5, the line ratios can be predicted for a number of ionization fractions and compared with the measured quantities; this is done in Figure 4. The variations of the [S II]/[N II] line ratios in UGC 3326, NGC 3628, NGC 4013, and NGC 4217 (the large uncertainties in the data of UGC 2092 prevent us from making any statement for this object) cannot be simply explained by a temperature gradient with height. The abundance of N<sup>+</sup> relative to that of S<sup>+</sup> varies with heights, perhaps an indication that an additional source of ionization is present in these objects.

The positive gradients in the vertical [O III]/H $\alpha$  profiles of NGC 2820, NGC 4302, and NGC 5777 strongly suggest the presence of an additional source of ionization that becomes more influential at lower densities. This possibility has also been suggested to explain the line ratios in our Galaxy (Haffner et al. 1999; Reynolds et al. 1999) and a few other external galaxies (Collins & Rand 2001). The next section considers this scenario in more detail.

##### 4.3. Secondary Source of Ionization

A wide variety of secondary sources of ionization have been suggested to account for the line ratios in the eDIG (see references in §1). In this section we discuss the predictions from three of the possible scenarios and compare them to our data. The promising possibility that cooling supernova remnants also contribute to the ionization of the eDIG (Slavin, McKee, & Hollenbach 2000) is not discussed here because the predicted line ratios are not available in this case.

###### 4.3.1. Turbulent Mixing Layers

Slavin et al. (1993) model the turbulent mixing layer (TML) created by shear flows between hot and cold gas. This layer is made up of intermediate-temperature gas which radiatively cools until the cooling rate is balanced by the energy flux into the gas layer. The properties of the TML depend on two main parameters, namely the temperature attained by the gas immediately after mixing and the enthalpy flux per particle into the layer (which itself depends on the velocity of the hot gas,  $v_t$ ). Their models span a temperature range of  $5.0 \leq \log T \leq 5.5$  and

a velocity range of  $25 \text{ km s}^{-1} \leq v_t \leq 100 \text{ km s}^{-1}$ . In their models, Slavin et al. assume pressure and ionization equilibrium between the hot and cold gas phases and slow mixing within the turbulent layer, so as to distinguish between turbulent mixing and shocks.

In general, the TML models are successful at predicting many of the observed line ratios, such as  $[\text{N II}]/\text{H}\alpha$  and  $[\text{S II}]/\text{H}\alpha$ . The TML models also predict strong  $[\text{O III}]/\text{H}\alpha$  emission (due to the high level of ionization in the mixing layer region), an emission line which is difficult to explain with photoionization alone (§4.1).

Figure 6 presents plots of the  $[\text{S II}]/\text{H}\alpha$ ,  $[\text{O III}]/\text{H}\alpha$  and  $[\text{O I}]/\text{H}\alpha$  line ratios versus  $[\text{N II}]/\text{H}\alpha$  for each of the galaxies in the sample. In the first column, the predicted values of the line ratios based on Sokolowski's photoionization model (using an absorption-hardened ionizing spectrum and dust-depleted abundances in the gas phase) are represented by a series of points connected by a thin solid line. The open triangles in these panels represent the predictions from Slavin et al.'s dust-depleted abundance TML models. Best-fit hybrid models that linearly combine the line ratio predictions from pure photoionization and pure TML models are shown as the thick solid line. The best fit is determined visually as the set of points that most closely match the data points in all three plots.

Of the three lefthand panels in Figure 6, the most informative is arguably the  $[\text{O III}]/\text{H}\alpha$  vs.  $[\text{N II}]/\text{H}\alpha$  diagram. The three TML models are clearly separated in this diagnostic diagram. In the other two panels, the predictions for the  $\log T = 5.3$  and the  $\log T = 5.5$  models are too close together to distinguish between the two models. Unfortunately, extended  $[\text{O III}]/\text{H}\alpha$  emission has not been detected in many of the galaxies, so our analysis of the hybrid photoionization/TML models based on the  $[\text{O III}]/\text{H}\alpha$  ratio is limited. The extraplanar  $[\text{O III}]/\text{H}\alpha$  profiles in the five galaxies in which  $[\text{O III}]/\text{H}\alpha$  has been detected fall into two categories: three objects show an increasing  $[\text{O III}]/\text{H}\alpha$  line ratio with increasing  $|z|$ , while the  $[\text{O III}]/\text{H}\alpha$  ratio drops with height in the other two galaxies. The galaxies in the first category tend to be better fit by a TML model with an intermediate mixing temperature ( $\log T = 5.3$ ), while those in the second category are better fit by a model with lower mixing temperatures ( $\log T = 5.0$ ).

For five of the galaxies in our sample, we find that the influence of the TML regions on the emission-line spectra increases with height, such that the contribution to the observed line ratios (*not* to the line flux) increase roughly from  $\sim 30$  to  $\sim 75\%$ . These results are consistent with models in which turbulent mixing occurs at higher elevations, where superbubbles break out of the thin disk layer, or at the locations where cooling halo gas is mixing with the ejected gas. There are exceptions to this general rule, however. In UGC 2092 and NGC 4013, the TML model contributes to the observed line ratios a near constant amount (70% and 40%, respectively), while in NGC 4217, the importance of the TML model appears to decrease with height (from 40% to 20%). Finally, one of the galaxies in our sample (NGC 4302) demonstrates only little deviations from the photoionization model, and these deviations are not well explained by any of the TML models.

#### 4.3.2. Shocks

Shull and McKee (1979) model interstellar radiating shocks such as those due to supernovae events. They include the ionizing effect of the UV precursor in the preshock gas in an effort

to make their models self-consistent. In their study, Shull and McKee discuss ten models. In seven of the models they choose as their standard preshock conditions a hydrogen particle density of  $10 \text{ cm}^{-3}$ , a magnetic field  $B_{0\perp} = 1 \mu\text{G}$  perpendicular to the flow, and cosmic metal abundances. They vary the shock velocity from 40 to  $130 \text{ km s}^{-1}$ . In the other three, they fix the shock velocity at  $100 \text{ km s}^{-1}$  and vary, in turn, the density, magnetic field, and metal abundances.

In the middle column of Figure 6, the predicted line ratios from the shock models of Shull & McKee are compared with the predictions from the photoionization model (Sokolowski 1994). The solar abundance shock models are represented by the open triangles (the solid triangle represents Shull and McKee's shock model with depleted abundances), while the photoionization models are represented by points joined by a thin solid line. The hybrid photoionization/shock model that best fits the data is shown as the dark solid line. The models of Shull & McKee with shock velocities near  $100 \text{ km s}^{-1}$  do well in predicting the high  $[\text{O III}]/\text{H}\alpha$  ratios detected in most eDIG and the relatively small  $[\text{O I}]/\text{H}\alpha$  ratios. The biggest problem arises when trying to model the galaxies which show a decreasing  $[\text{O III}]/\text{H}\alpha$  line ratio with increasing  $|z|$  (recall that two out of five galaxies with detected extraplanar  $[\text{O III}]/\text{H}\alpha$  show this behavior). In these galaxies, the  $[\text{O III}]/\text{H}\alpha$  ratio drops below that which is predicted by the pure photoionization model. Since all of the shock models predict enhanced  $[\text{O III}]/\text{H}\alpha$  line ratios, they are unable to explain the negative  $[\text{O III}]/\text{H}\alpha$  vertical gradients.

In galaxies without extraplanar  $[\text{O III}]/\text{H}\alpha$  data, we have to rely heavily on the  $[\text{S II}]/\text{H}\alpha$  vs.  $[\text{N II}]/\text{H}\alpha$  plot to determine the best fitting models. The line ratios for NGC 3628 and NGC 4013 can hardly be explained by a combination of shocks and photoionization (shocks can contribute at most  $\sim 10\%$  to the observed line ratios). In the other galaxies, the best-fitting model appears to be the depleted abundances model with a shock velocity of  $100 \text{ km s}^{-1}$ . In general, the influence of the shocks on the observed line ratios appears to increase with increasing heights (from  $\sim 10 - 20\%$  near the disk of the galaxies up to  $\sim 40 - 60\%$  at higher  $|z|$ ). In at least three of the galaxies, the hybrid photoionization/shock model seems to imply that the ionization parameter decreases from a value of  $\log U = -3$  near the plane of the galaxy down to  $\log U = -4$  at heights  $|z| \gtrsim 1 \text{ kpc}$ .

#### 4.3.3. Shock + Precursor

In a pair of papers, Dopita and Sutherland (1995, 1996) present a grid of models of low-density, high-velocity photoionizing radiative shocks. Dopita and Sutherland model photons which propagate both upstream through the preshock gas as well as downstream into the recombination region of the shock. Their grid spans a broad range in shock velocity and magnetic parameter,  $B/n_e^{1/2}$ . They assume solar abundances and a low-density radiative steady flow shock. The importance of the magnetic parameter comes into play because they assume that the magnetic field is frozen into the flow. Dopita and Sutherland present models both with and without precursor regions.

In these models, an increase in the shock velocity causes an increase in the ionization parameter in the pre-shock gas. Since the postshock plasma is the source of ionizing photons in radiative shocks, the faster the shock the larger the flux of ionizing photons, and hence the higher the ionizing parameter. Dopita and Sutherland also found that an increase in the magnetic parameter increases the ionization parameter in

the photoionization-recombination zone of the shock, since the electron density is inversely proportional to the magnetic parameter, and the ionization parameter is inversely proportional to the electron density.

The predictions from Dopita and Sutherland's shock models are shown in the right column of Figure 6. The grid spans a range in shock velocity from 100 to 500 km s<sup>-1</sup> (the 500 km s<sup>-1</sup> line is represented by a dashed line) and a range in the magnetic parameter  $B/n_e^{1/2}$  from 0 to 4  $\mu\text{G cm}^{3/2}$  (the 4  $\mu\text{G cm}^{3/2}$  line is represented by a dotted line). Due to the large parameter space represented by the Dopita and Sutherland shock models, it is difficult to say with much certainty the exact parameters that are needed to reproduce the observed line ratios. In general, it appears that models combining photoionization and shocks with no precursor do better in reproducing the line ratios than those using the shocks + precursor models. The measured ratios also seem to indicate an increase in the shock velocity with increasing height.

### 5. SUMMARY

Deep long-slit spectra reaching flux levels of a few  $10^{-18}$  erg s<sup>-1</sup> cm<sup>-2</sup> arcsec<sup>-2</sup> were obtained of nine nearby, edge-on spiral galaxies. H $\alpha$ , [N II]  $\lambda\lambda 6583$ , and [S II]  $\lambda\lambda 6716, 6731$  are detected out to a few kpc in all of these galaxies. Several other fainter diagnostic lines are also detected over a slightly smaller scale. The relative strengths, centroids, and widths of the various emission lines provide constraints on the electron density, temperature, reddening, kinematics, and possible source(s) of ionization of the eDIG. The main conclusions from the analysis are the followings:

- Seven of the nine galaxies in the sample show a general increase in the [N II]/H $\alpha$  and [S II]/H $\alpha$  line ratios with increasing height. The extraplanar [N II]/H $\alpha$  line ratios reach values in excess of 1.5 in some galaxies. Extraplanar [O III] line emission has been reliably detected in five galaxies, and three of those show an increasing [O III]/H $\alpha$  line ratio with height. Extraplanar [O I] line emission has been detected in three of the galaxies, and in each case, the [O I]/H $\alpha$  line ratio increases with increasing  $|z|$ . These trends in the line ratios are similar to those observed in other galaxies including our own.
- He I  $\lambda 5876$  is detected in the midplane of four of the galaxies, with values ranging from 0.018 to 0.052. This suggests an effective stellar temperature range of 36,500 – 38,500 K and an upper limit to the stellar mass function of 42 – 54  $M_\odot$ . Extraplanar He I emission is detected in only one galaxy, NGC 2820. The He I/H $\alpha$  and [N II]/H $\alpha$  line ratios in the eDIG of this galaxy are consistent with O-star photoionization, although the other ratios in this galaxy suggest the presence of an additional source of ionization.
- For all but one galaxy in the sample (NGC 4302), photoionization by massive OB stars does not appear to be sufficient to explain the line ratios in the eDIG. At least one other source of ionization appears to be needed. Hybrid models that combine photoionization by OB stars and photoionization by turbulent mixing layers (TMLs) or shocks provide the best fit to the data. In contrast to the pure photoionization models, these hybrid models are able to reproduce the run in the [O III]/H $\alpha$  line

ratios observed in many of the galaxies. Overall, the hybrid photoionization/TML models do a better job of explaining the observed line ratios than the photoionization/shock models, although in many cases the photoionization/shock models do almost or just as well. The contribution of the turbulent mixing layers (or shocks) to the observed line ratios appears to increase with increasing height. These results are consistent with models in which turbulent mixing and shocks occur at higher elevations, where superbubbles break out of the thin disk layer, or at the locations where cooling halo gas is mixing with the ejected gas.

- Three galaxies in the sample appear to show significant vertical velocity gradients. In NGC 3628, the presence of a prominent dust lane is affecting the velocity measurements and producing large variations in excess of 100 km s<sup>-1</sup> within a range in height of only 0.5 kpc. Monotonic velocity gradients of order 50 – 70 km s<sup>-1</sup> kpc<sup>-1</sup> appear to exist in NGC 2820 and NGC 4013 (a gradient may also be present in NGC 4302, but the uncertainties are large). These gradients can be explained if the rotational velocities of the eDIG are lower in the eDIG than in the disk, as predicted by the galactic fountain model. The upper limits on the velocity gradients in the other galaxies ( $\sim 30 - 50$  km s<sup>-1</sup> depending on the galaxy) are not inconsistent with this model.

This work has benefitted from several discussions with J. Bland-Hawthorn. The authors thank the referee, Dr. René Walterbos, for several suggestions which significantly improved this paper. SV is indebted to the California Institute of Technology and the Observatories of the Carnegie Institution of Washington for their hospitality, and is grateful for partial support of this research by a Cottrell Scholarship awarded by the Research Corporation, NASA/LTSA grant NAG 56547, and NSF/CAREER grant AST-9874973. STM was also supported in part by NSF/CAREER grant AST-9874973. This work has made use of NASA's Astrophysics Data System Abstract Service and the NASA/IPAC Extragalactic Database (NED), which is operated by the Jet Propulsion Laboratory, California Institute of Technology, under contract with the National Aeronautics and Space Administration.

### Appendix: Notes on Individual Objects

#### UGC 2092

This is a highly inclined ( $i = 86^\circ$ ; Guthrie 1992) Scd galaxy that lies at a distance of 72 Mpc (PBS). PBS detected a bubble-like structure approximately  $20''$  NE in the plane of the galaxy. We positioned the slit so that it passes directly through this structure (Fig. 1). UGC 2092 is the most distant galaxy in the sample. In order to detect even the strongest emission lines, the

data were spatially binned by a factor of two, yielding a spatial scale of  $\sim 1.1$  kpc per spatial element. The TML models have difficulties explaining the observed line ratios. Higher mixing gas temperatures seem to be favored, but if this were the case, then the TML model would have to account for almost all of the observed emission on the west side of the galaxy, while the east side would require an ionization parameter smaller than  $-5.0$ . The shock models do a better job of explaining the observed line ratios. A shock velocity of  $100 \text{ km sec}^{-1}$  and depleted abundances appear to best model the shock environment. According to the  $[\text{S II}]/\text{H}\alpha$  vs.  $[\text{N II}]/\text{H}\alpha$  plot, shocks play a more important role on the east side of the galaxy, contributing about 60% to the observed line ratios, while on the west side, only 15% – 45% of the observed line ratios is produced through shocks. Dopita & Sutherland’s shock models also suggest a stronger influence from shocks on the eastern side of the galaxy. The observed line ratios can best be modeled by emission originating in the recombination region of the shock, with a magnetic parameter of  $\sim 0 \mu\text{G cm}^{3/2}$ .

### UGC 3326

UGC 3326 is a Scd galaxy which lies at a distance of 48 Mpc (PBS) with an inclination angle of  $90^\circ$  (Guthrie 1992). PBS detected a faint plume on the SW side of the galaxy. The plume extends outward at an angle of  $52^\circ$  away from the axis of the galaxy out to a height  $\sim 1.3$  kpc. At the end of the plume is a relatively bright cloudlike structure. The slit was centered on the galaxy and ran directly through this plume (Fig. 1). UGC 3326 also required 2x spatial binning in order to detect even the strongest emission lines, yielding a spatial scale of  $\sim 700$  pc per spatial element. As in the case of UGC 2092, only  $[\text{N II}]/\text{H}\alpha$  and  $[\text{S II}]/\text{H}\alpha$  are available to estimate the influence of a secondary source of ionization. The observed line ratios near the disk of the galaxy (out to  $\sim 700$  pc) are consistent with the photoionization model and do not require a secondary ionization source. At higher  $|z|$  (on the northwest side of the galaxy), however, the  $[\text{S II}]/\text{H}\alpha$  line ratios are larger than what can solely be explained by the photoionization model. The TML model suggests that at higher elevations, about 40 – 80% of the line ratios is produced by the mixing layer gas, while the shock model suggests that 20 – 40% of the line ratio arises from shocks (based on the  $100 \text{ km sec}^{-1}$ , depleted abundances model). Unfortunately, with only  $\text{H}\alpha$ ,  $[\text{N II}]$  and  $[\text{S II}]$  lines observed in this galaxy, we cannot further constrain the data or verify which model best explains the observed eDIG emission.

### UGC 4278

R96 imaged UGC 4278, an SB(s)d galaxy with an inclination of  $90^\circ$  (Tully 1988), and detected prominent plumes on both sides of the nucleus of the galaxy, out to a height of  $\sim 1.4$  kpc. R96 suggests that this may trace outflow from a nuclear starburst. Our slit was positioned so it passes through the nucleus of the galaxy, and therefore through the emission-line regions detected by R96 (Fig. 1). UGC 4278 lies at a distance of 10.6 Mpc (Tully 1988), yielding a spatial scale of  $\sim 160$  pc  $\text{pixel}^{-1}$ . The  $[\text{O III}]/\text{H}\alpha$  data in UGC 4278 tend to complicate the identification of the secondary source of ionization. While

the data for this line ratio, as well as  $[\text{S II}]/\text{H}\alpha$ , suggest the need for an additional source of ionization, they conflict in the determination of exactly what that secondary source might be. While the  $[\text{S II}]/\text{H}\alpha$  line ratio shows a general increase with height, the  $[\text{O III}]/\text{H}\alpha$  line ratio show a general decrease with height. While the  $[\text{S II}]/\text{H}\alpha$  vs.  $[\text{N II}]/\text{H}\alpha$  data points may be explained with a photoionization model with ionization parameters from  $\sim -2.0$  to  $-3.0$  mixed with shocked gas with a shock velocity of  $100 \text{ km sec}^{-1}$  in a depleted abundance region, neither this model nor any other shock model can explain the decrease in the  $[\text{O III}]/\text{H}\alpha$  line ratio with increasing height. Similar problems occur with the TML models. While the TML models with low mixing gas temperatures (such as  $\log T = 5.0$ ) have negligible  $[\text{O III}]$  emission, and so could account for a decrease in this line relative to  $\text{H}\alpha$  if TML becomes more important at large heights, the predicted  $[\text{S II}]/\text{H}\alpha$  and  $[\text{N II}]/\text{H}\alpha$  line ratios for this model lie close to the photoionization curve, and so limits the available parameter space. Looking at Figure 6, the observed  $[\text{S II}]/\text{H}\alpha$  and  $[\text{N II}]/\text{H}\alpha$  ratios are clearly larger than predicted by any combinations of O-star photoionization and  $\log T = 5.0$  TML models.

The remarkably small  $[\text{N II}]/\text{H}\alpha$  line ratios in the disk of this galaxy have been noted previously by Goad & Roberts (1981). In their study of superthin galaxies, one of which was UGC 4278, they derive a mean  $[\text{N II}]/\text{H}\alpha$  line ratio of 0.12 for this object, consistent with our measurements. They conclude that the small  $[\text{N II}]/\text{H}\alpha$  ratios are a result of nitrogen deficiency in this galaxy. This suggests that star formation proceeds on a much longer time scale than in most galaxies, since nitrogen is a secondary product of nucleosynthesis. It also implies that large-scale shocks are rare in UGC 4278.

### NGC 2820

NGC 2820 lies at a distance of 20 Mpc, yielding a spatial scale of  $\sim 300$  pc  $\text{pixel}^{-1}$ . The position of the slit was selected based on the narrowband images reported in Paper I. As discussed in §3.1.2, NGC 2820 is the only galaxy in our sample where extraplanar  $\text{He I}/\text{H}\alpha$  emission has been detected out to  $|z| \sim 1$  kpc. It is also the only galaxy in which all four main line ratios are detected out to large vertical heights, therefore providing strong constraints on the nature of secondary ionization source. The main concern with NGC 2820 is that the majority of the  $[\text{O III}]/\text{H}\alpha$  vs.  $[\text{N II}]/\text{H}\alpha$  data points lie below the photoionization curve. The TML models with low mixing gas temperatures ( $\log T = 5.0$ ) also have low  $[\text{O III}]/\text{H}\alpha$  values. Using this model in conjunction with the photoionization model, the  $[\text{O III}]/\text{H}\alpha$  and  $[\text{O I}]/\text{H}\alpha$  data suggest that turbulent mixing layers contribute roughly 35 – 55% to the observed line ratios. Unfortunately, the  $[\text{S II}]/\text{H}\alpha$  data do not support this conclusion. The  $[\text{S II}]/\text{H}\alpha$  data suggest a higher mixing gas temperature ( $\log T = 5.3$ ), with the contribution to the line ratios arising from this region apparently increasing with heights from 20 to 80%. The comparison with the photoionization/shock hybrid model suggests that the data are best fit by the model with shock velocity  $v_s = 100 \text{ km sec}^{-1}$  and depleted abundance. With the exception of those  $[\text{O III}]/\text{H}\alpha$  data points that fall below the photoionization curve, the remaining data suggest that the ionization parameter decreases from  $\sim -3.0$  to  $-4.0$  while the contribution of shocks to the line ratios rises from  $\sim 10$  to



40%. The Dopita & Sutherland models are perhaps more successful at explaining the observed trends in the line ratios. The  $[\text{N II}]/\text{H}\alpha$ ,  $[\text{S II}]/\text{H}\alpha$ , and  $[\text{O III}]/\text{H}\alpha$  line ratios lie in the region of the (shock + precursor) model with a magnetic parameter of  $\sim 0 \mu\text{G cm}^{3/2}$ .

### NGC 3628

NGC 3628 is a starbursting Sb galaxy which is a member of the Leo Triplet. Located at a distance of 6.7 Mpc, it has an inclination angle of  $87^\circ$  (Tully 1988). Imaged by Fabbiano, Heckman, and & Keel (1990), they detected a large plume extending about 9 kpc from the west side of the galaxy (see also Dahlem et al. 1996). It is not exactly perpendicular to the disk of the galaxy, but lies at a position angle of  $210^\circ$  (while the disk of the galaxy lies at a position angle of  $104^\circ$ ). In order to cover as much of this plume as possible, we positioned the slit to extend only to vertical heights to the south side of the disk, following the extent of the plume, rather than centered on the disk of the galaxy (see Fig. 1). Fabbiano et al. also obtained spectroscopic information along the minor axis of NGC 3628, though not through the detected plume. They detected a midplane  $[\text{N II}]/\text{H}\alpha$  ratio of 0.4 which increased to  $> 1.0$  at higher  $|z|$ .  $[\text{S II}]/\text{H}\alpha$  was also detected and observed to increase with  $|z|$ , having a midplane value of 0.3 and rising to  $\sim 0.8$  at large heights. Shock ionization was proposed by Fabbiano et al. (1990) to explain these line ratios. Figure 6 shows that pure shock or photoionization/shock hybrid models are unable to reproduce the small  $[\text{O III}]/\text{H}\alpha$  line ratios in the extraplanar plume; this is different from the conclusion of Fabbiano et al (1990) who did not have constraints on the  $[\text{O III}]$  emission. The photoionization/TML hybrid models with a mixing gas temperature of  $\log T = 5.0$  are more successful at explaining the observations. Based on this model, the TML region would contribute roughly 50% to the observed line ratios, although the exact amount differs between the  $[\text{O III}]/\text{H}\alpha$  and  $[\text{S II}]/\text{H}\alpha$  data points. The plume may represent the interface where hot wind gas mixes with entrained disk material (Dahlem et al. 1996).

### NGC 4013

NGC 4013 is a Sb galaxy at a distance of 17 Mpc (260 pc  $\text{pixel}^{-1}$ ; Tully 1988) and with an inclination of  $90^\circ$  (Bottema 1995). R96 detects extraplanar gas features extending up to  $|z| \sim 2.5$  kpc on the northeast side, as well as a less prominent line-emitting region on the southwest side. Our recent imaging study (Paper I) confirms the presence of eDIG in this object. We positioned our slit to cover the northeast region. The photoionization/TML hybrid model with  $\log T = 5.0$  works well for NGC 4013. While there are only a few  $[\text{O III}]/\text{H}\alpha$  data points, they are consistent with the  $[\text{S II}]/\text{H}\alpha$  data points, suggesting an ionization parameter of  $\sim -3.8$  and implying that approximately 50% of the line ratios originate from the TML region. The photoionization/shock hybrid model is unable to reproduce the observed emission-line ratios.

### NGC 4217

NGC 4217 is a Sb galaxy at a distance of 17 Mpc (260 pc  $\text{pixel}^{-1}$ ; Tully 1988) with an inclination of  $86^\circ$  (R96). R96 detects two bright plumes of extraplanar emission extending  $\sim 2$  kpc from either side of the disk on the southwest side of NGC 4217. Our slit was positioned so that it passes through both plumes of extraplanar gas.  $[\text{O I}]$  was detected out to  $\sim 1.3$  kpc on either side of NGC 4217. Based on the  $[\text{O I}]/\text{H}\alpha$  line ratios, in addition to the observed  $[\text{S II}]/\text{H}\alpha$  line ratios, we find that the photoionization/TML hybrid models predict that the ionization parameter decreases from  $-4.0$  to  $-5.0$ , while the influence of TMLs on the observed line ratios remains relatively constant at  $\sim 40\%$ . The best fit photoionization/shock model suggests an ionization parameter which decreases from  $-3.5$  to  $-4.8$ , and a shock model with a velocity of  $100 \text{ km sec}^{-1}$  and depleted abundances, which provides only 10 to 20% of the observed line ratios. According to the Dopita & Sutherland shock models, the observed emission is inconsistent with shock + precursor emission. Although there is significant scatter in the data, the observed line ratios appear to be well described by emission originating from a region with a magnetic parameter  $< 1 \mu\text{G cm}^{3/2}$  and a shock velocity which increases with increasing height (up to almost  $400 \text{ km sec}^{-1}$ ).

### NGC 4302

NGC 4302 was imaged by both R96 and PBS. It is an Sc galaxy at a distance of 16.8 Mpc (250 pc  $\text{pixel}^{-1}$ ; Tully 1988) with an inclination of  $90^\circ$  (R96). PBS detected an extremely faint emission-line structure emerging 0.73 kpc from the plane close to the nucleus of the galaxy. R96 detects faint, diffuse extraplanar emission at galactocentric radii  $< 4$  kpc up to  $|z| \sim 2$  kpc. Therefore, we chose to place our slit through the center of the galaxy to incorporate both structures. Unfortunately, the uncertainties on many of the extraplanar line ratios are large and prevent us from making strong statements on the source of ionization in the eDIG of NGC 4302. All of the data points are consistent with the photoionization model, within the large measurement errors.

NGC 4302 was also observed spectroscopically by Collins & Rand (2001). The position of their slit is  $20''$  southeast of ours, or given a distance of 16.8 Mpc,  $\sim 1.6$  kpc southeast. They detect the prominent  $[\text{N II}]$  and  $[\text{S II}]$  lines up to  $z = 2$  kpc on either side of the galaxy, but poor weather conditions prohibited the detection of  $[\text{O III}]$ . Their  $[\text{N II}]/\text{H}\alpha$  line ratios increase from 0.4 up to 1.4 at  $|z| = 1.5$  kpc, and their detected  $[\text{S II}]/[\text{N II}]$  line ratios remain constant at  $\sim 0.6$ . These values suggest a gas temperature ranging from 6600 to 10,000 K. While their line ratios differ from ours, we do see the same general increase in the emission line ratios with  $|z|$ .

### NGC 5777

In NGC 5777, an Sb galaxy with an inclination of  $83^\circ$  (Guthrie 1992) located at a distance of 25 Mpc (380 pc  $\text{pixel}^{-1}$ ; PBS), PBS detected a prominent extraplanar plume extending 1.1 kpc directly north-east from a bright H II region located on the southeast side of the galaxy. We positioned our slit so that it was centered on the galaxy disk and passed through this plume.

A photoionization/TML hybrid model with a mixing gas temperature of  $\log T = 5.3$  best fits the data. This fit suggests that the ionization parameter decreases from  $-4.0$  to  $-5.0$  while the contribution from the TML region to the emission line ratios increases from  $\sim 20$  to  $80\%$ . The photoionization/shock hybrid model is less successful at explaining the data. The best fit is found with a model with a shock velocity of  $100 \text{ km sec}^{-1}$  and depleted abundances, where the contribution from the shock

models to the emission line ratios increases from  $\sim 15$  to  $40\%$  with increasing heights. The Dopita & Sutherland models also have difficulties reproducing the data. The  $[\text{O III}]/\text{H}\alpha$  ratios measured at high  $|z|$  favor a shock + precursor model, while the  $[\text{S II}]/\text{H}\alpha$  data suggest that the emission originates from shocks without precursor. These ratios also suggest different values for the magnetic parameter.

## REFERENCES

- Baldwin, J. A., Phillips, M. M., & Terlevich, R. 1981, *PASP*, 93, 5  
 Bland-Hawthorn, J., Freeman, K. C., Quinn, P. J., 1997, *ApJ*, 490, 143  
 Boesgaard, A. M., & Steigman, G. 1985, *ARA&A*, 23, 319  
 Bottema, R., 1995, *A&A*, 295, 605  
 Bregman, J. 1980, *ApJ*, 236, 577  
 Brockelhurst, M. 1972, *MNRAS*, 157, 211  
 Collins, J. A., Benjamin, R. A., & Rand, R. J. 2002, *ApJ*, 578, 98  
 Collins, J. A., & Rand, R. J. 2001, *ApJ*, 551, 57  
 Dahlem, M. 1997, *PASP*, 109, 1298  
 Dahlem, M., Heckman, T. M., Fabbiano, G., Lenhart, M. D., & Gilmore, D. 1996, *ApJ*, 461, 724  
 de Vaucouleurs, G., de Vaucouleurs, A., Corwin, H. G., Buta, R. J., Paturel, G., & Fouqué, P., 1991, *Third Catalogue of Bright Galaxies*, Springer, New York  
 Dettmar, R.-J. 1992, *Fund. Cosmic Physics*, 15, 143  
 Dettmar, R.-J., & Schultz, H. 1992, *A&A*, 254, L25  
 Domgörgen, H., & Dettmar, R.-J., 1997, *A&A*, 322, 391  
 Domgörgen, H., & Mathis, J. S. 1994, *ApJ*, 428, 647  
 Dopita, M. A., Kewley, L. J., Heisler, C. A., & Sutherland, R. S. 2000, *ApJ*, 542, 224  
 Dopita, M. A., & Sutherland, R. S., 1995, *ApJ*, 455, 468  
 —, 1996, *ApJS*, 102, 161  
 Evans, I. N., & Dopita, M. A. 1985, *ApJS*, 58, 125  
 Fabbiano, G., Heckman, T., & Keel, W. C., 1990, *ApJ*, 355, 442  
 Ferguson, A., Wyse, R., & Gallagher, J. 1996, *AJ*, 112, 2567  
 Goad, J. W., & Roberts, M. S. 1981, *ApJ*, 250, 79  
 Golla, G., Dettmar, R.-J., & Domgörgen, H., 1996, *A&A*, 313, 439  
 Guthrie, B. N. G., 1992, *A&AS*, 93, 255  
 Haffner, L. M., Reynolds, R. J., & Tufte, S. L. 1999, *ApJ*, 523, 223  
 Hartquist, T. W., & Morfill, G. E. 1986, *ApJ*, 311, 518  
 Houck, J. C., & Bregman, J. N. 1990, *ApJ*, 352, 506  
 Hummel, E., & van der Hulst, J. M. 1989, *A&AS*, 81, 51  
 Kaler, J. B. 1976, *ApJS*, 31, 517  
 Keppel, J. W., Dettmar, R.-J., Gallagher, J. S., & Roberts, M. S. 1991, *ApJ*, 374, 507  
 Lerche, I., & Schlickeiser, R. 1982 *A&A*, 107, 148.  
 Martin, P. G. 1988, *ApJS*, 66, 125  
 Mathis, J. S. 1986, *ApJ*, 301, 423  
 —, 2000, *ApJ*, 544, 347  
 McCall, M. L., Rybski, P. M., & Shields, G. A. 1985, *ApJS*, 57, 1  
 Meyer, D. M., Cardelli, J. A., & Sofia, U. J. 1997, *ApJ*, 490, L103  
 Miller, S. T., & Veilleux, S. 2003a, *ApJS*, submitted (Paper I)  
 Osterbrock, D., 1989, *Astrophysics of Gaseous Nebulae and Active Galactic Nuclei* (Mill Valley: University Science)  
 Osterbrock, Tran, & Veilleux 1992, *ApJ*, 389, 196  
 Otte, B., & Dettmar, R.-J., 1999, *A&A*, 343, 705  
 Otte, B., Gallagher, J. S., & Reynolds, R. J. 2002, *ApJ*, 572, 823  
 Otte, B., Reynolds, R. J., Gallagher, J. S., & Ferguson, A. M. N. 2001, *ApJ*, 560, 207  
 Parker, E. N. 1992, *ApJ*, 401, 137.  
 Pildis, R. A., Bregman, J. N., & Schombert, J. M. 1994a, *ApJ*, 423, 190  
 —, 1994b, *ApJ*, 427, 160 (PBS)  
 Rand, R. J. 1996, *ApJ*, 462, 712 (R96)  
 —, 1997, *ApJ*, 474, 129  
 —, 1998, *ApJ*, 501, 137  
 —, 2000, *ApJ*, 537, 13  
 Rand, R. J., Kulkarni, S. R., & Hester, J. J. 1990, *ApJ*, 352, L1 (erratum 362, L35)  
 Raymond, J. C. 1992, *ApJ*, 384, 502  
 Reynolds, R. J. 1984, *ApJ*, 282, 191  
 —, 1985a, *ApJ*, 294, 256  
 —, 1985b, *ApJ*, 298, L27  
 —, 1992, *ApJ*, 392, L35  
 Reynolds, R. J., Haffner, L. M., & Tufte, S. L. 1999, *ApJ*, 525, L21  
 Reynolds, R. J., Sterling, N. C., Haffner, L. M., & Tufte, S. L. 2001, *ApJ*, 548, 221  
 Reynolds, R. J., & Tufte, S. L. 1995, *ApJ*, 439, L17  
 Shull, J. M., & McKee, C. F., 1979, *ApJ*, 227, 131  
 Slavin, J., McKee, C., & Hollenbach, D., 2000, *ApJ*, 541, 218  
 Slavin, J. D., Shull, J. M., & Begelman, M. C. 1993, *ApJ*, 407, 83  
 Sokolowski 1994, PhD thesis, Rice University  
 Stasinski, G. 1982, *A&AS*, 48, 299  
 Tüllman, R. & Dettmar, R.-J. 2000, *A&A*, 362, 119  
 Tüllman, R., Dettmar, R.-J., Soida, M., Urbanik, M., & Rossa, J. 2000, *A&A*, 364, L36  
 Tully, R. B., 1988, *Nearby Galaxies Catalog* (Cambridge: Cambridge University Press)  
 Veilleux, S. 2001, in *IAU Coll. 184, AGN Surveys*, eds. R.F. Green, E.Ye. Khachikian, and D.B. Sanders, *ASP Conf. Series.*, in press (astro-ph/0201118)  
 Veilleux, S., Cecil, G., & Bland-Hawthorn, J. 1995, *ApJ*, 445, 152  
 Veilleux, S., & Osterbrock, D. E. 1987, *ApJS*, 63, 295

FIG. 1.— Position of the slit superposed on the continuum-subtracted  $H\alpha$  image of (a) the NE side of UGC 2092, (b) the SW side of UGC 3326, (c) UGC 4278, (d) NGC 2820, (e) NGC 3628, (f) NGC 4013, (g) NGC 4217, (h) NGC 4302 and (i) NGC 5777 (see Table 1 for references to the images). The position of the slit is chosen to pass through at least one known region of eDIG. In most cases the slit is positioned perpendicular to the plane of the galaxy. In the others, it is positioned to maximize coverage of the eDIG. UGC 2092 is rotated clockwise by  $32^\circ$  such that the disk of the galaxy runs vertically, while UGC 3326 was rotated clockwise by  $84^\circ$ . The other figures have not been rotated (North is at the top of the figure and east to the left).

FIG. 2.— Emission line spectra as a function of position along the slit. For display purposes, the spectra are scaled individually (or in sets of two or three) with the scaling factor in relation to the spectrum containing the  $H\alpha + [N II]$  complex listed in the upper right corner of each spectrum. The expected redshifted positions of the emission lines as determined from the systemic velocity of the galaxies are indicated by the dashed lines. Tickmarks on the horizontal axis are separated by  $25 \text{ \AA}$  in the observer's restframe. In the cases where no line is detected, a representative spectrum from near the disk of the galaxy is presented. The presence of the Na ID  $\lambda\lambda 5897.6, 5891.6$  absorption lines near He I is apparent in some of the galaxies (e.g., NGC 3628, NGC 4217, NGC 4302 and UGC 3326).

FIG. 3.— Vertical profiles of  $[N II] \lambda 6583/H\alpha$ ,  $[S II] \lambda 6716/H\alpha$ ,  $[S II] \lambda 6716/[N II] \lambda 6583$ ,  $[O III] \lambda 5007/H\alpha$ ,  $[O I] \lambda 6300/H\alpha$ , He I  $\lambda 5876/H\alpha$ ,  $H\alpha/H\beta$ ,  $[S II] \lambda 6716/[S II] \lambda 6731$ , and  $[O III] \lambda 5007/[O III] \lambda 4959$ . This last ratio is expected to be constant ( $\sim 3$ ) within the uncertainties. The error bars represent one- $\sigma$  uncertainties. Also shown in each panel are the spatial profiles of the  $H\alpha$  emission (solid line) and continuum emission (dashed line), both of which have been arbitrarily scaled for display purposes. Only ratios involving detected lines have been included in this figure.

FIG. 4.— Temperature profile and ionization fraction in the eDIG. In the bottom left panel is a plot of the temperature profile (in units of  $10^4 \text{ K}$ ) based on the  $[N II] \lambda 6583/H\alpha$  line ratio presented in the upper left panel [see eqn. (2)]. Using this temperature profile,  $[S II] \lambda 6716/H\alpha$ ,  $[S II] \lambda 6716/[N II] \lambda 6583$ ,  $[O III] \lambda 5007/H\alpha$  and  $[O I] \lambda 6300/H\alpha$  have been calculated and superimposed on the observed line ratios [see §4.2 and eqns. (3) through (6) for details]. The lines represent different ionization fractions ranging from 12.5% (first solid line) to 100% (last dotted line). The top two panels to the right of the  $[N II]/H\alpha$  plot represent the  $S^+/S$  ratio; the bottom, middle plot represents the  $O^{++}/O$  ratio; and the bottom, right plot represents the  $H^+/H$  ratio. The  $[N II]/H\alpha$  ratios cannot be used to derive the temperature profile in objects with strong eDIG  $[O III]/H\alpha$  ratios ( $\gtrsim 0.25$ ); four objects are therefore excluded from the analysis (UGC 4278, NGC 2820, NGC 4302, and NGC 5777; see text).

FIG. 5.— Velocity and line width profiles. In three of the panels, the velocity centroids of the  $H\alpha$ ,  $[N II] \lambda 6583$  and  $[S II] \lambda 6716$  emission lines are plotted as a function of position along the slit. The velocities are plotted relative to the systemic velocity in  $\text{km s}^{-1}$ . The dot-dashed line represents the average position of the line centroid. One- $\sigma$  error bars have been computed based on the accuracy in detecting the true line centroid as a function of signal-to-noise ratio. The bottom, right figure presents the measured  $H\alpha$  line widths in  $\text{km s}^{-1}$  as a function of vertical height. These measurements have been corrected for the width of the instrumental profile.

FIG. 6.— (a) Comparisons of observed  $[S II] \lambda 6716/H\alpha$ ,  $[O III] \lambda 5007/H\alpha$ ,  $[O I] \lambda 6300/H\alpha$ , and  $[N II] \lambda 6583/H\alpha$  line ratios with the predictions of photoionization, turbulent mixing layer, and shock models. The data for UGC 2092 are the filled circles with error bars. The series of points joined by a thin solid line in the panels in the left and middle columns represent the predictions from photoionization models of a hardened spectrum and dust depleted abundances with ionization parameters ( $\log U$ ) of  $-3.0, -3.5, -4.0, -4.2, -4.5$ , and  $-5.0$  (note that  $[N II]/H\alpha$  decreases with increasing  $\log U$ ; Sokolowski 1994). The left column overlays the predictions from the turbulent mixing layer (TML) models of Slavin et al. (1993). These values are derived from models with a hot gas velocity of  $25 \text{ km s}^{-1}$ , depleted abundances, and an intermediate temperature after mixing of  $\log T = 5.0$ ,  $\log T = 5.3$ , or  $\log T = 5.5$  (represented by open triangles with size increasing with temperature). The hybrid photoionization/TML model which best fits the data is shown as a thick solid line. This model incorporates TMLs with a mixing temperature of  $\log T = 5.5$  (see text for more detail). The middle column overlays shock model predictions from Shull & McKee (1979). The values plotted are calculated from solar abundance models with shock velocities of 90, 100, and  $110 \text{ km s}^{-1}$  (represented by open triangles of increasing size). A model with a shock velocity of  $100 \text{ km s}^{-1}$  and depleted abundances (filled triangle) is also shown for comparison. For this galaxy as well as the others, the best fit to the photoionization/shock hybrid model is derived using the shock model with depleted abundances. The panels in the right column presents the grid of predictions from the shock and shock+precursor solar abundance models of Dopita & Sutherland (1995). The shock velocity ranges from 100 to  $500 \text{ km s}^{-1}$  (the  $500 \text{ km s}^{-1}$  line is represented by a dashed line) and the magnetic parameter  $B/n_e^{1/2}$  ranges from 0 to  $4 \mu\text{G cm}^{3/2}$  (the  $4 \mu\text{G cm}^{3/2}$  line is represented by a dotted line). (b) Same as Figure 6a but for UGC 3326. The best fit for the photoionization/TML hybrid model uses a mixing temperature of  $\log T = 5.3$ . (c) Same as Figure 6a but for UGC 4278. The best fit for the photoionization/TML model uses a mixing temperature of  $\log T = 5.0$ . (d) Same as Figure 6a but for NGC 2820. The best fit for the photoionization/TML hybrid model uses a mixing temperature of  $\log T = 5.3$ . (e) Same as Figure 6a but for NGC 3628. The best fit for the photoionization/TML hybrid model uses a mixing temperature of  $\log T = 5.0$ . (f) Same as Figure 6a but for NGC 4013. The best fit for the photoionization/TML hybrid model uses a mixing temperature of  $\log T = 5.0$ . (g) Same as Figure 6a but for NGC 4217. The best fit for the photoionization/TML hybrid model uses a mixing temperature of  $\log T = 5.0$ . (h) Same as Figure 6a but for NGC 4302. These data do not require a secondary source of ionization. (i) Same as Figure 6a but for NGC 5777. The best fit for the photoionization/TML hybrid model uses a mixing temperature of  $\log T = 5.3$ .

FIG. 1.— See jpg image.

FIG. 1.— (Cont'd) See jpg image.

FIG. 1.— (Cont'd) See jpg image.

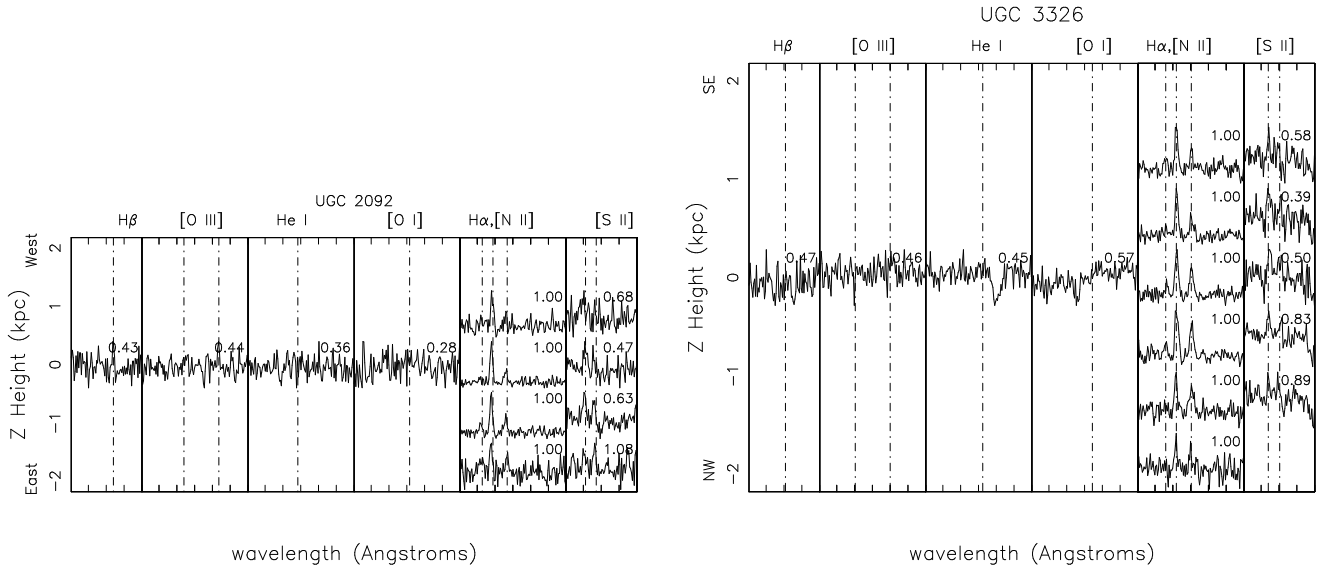


FIG. 2.—

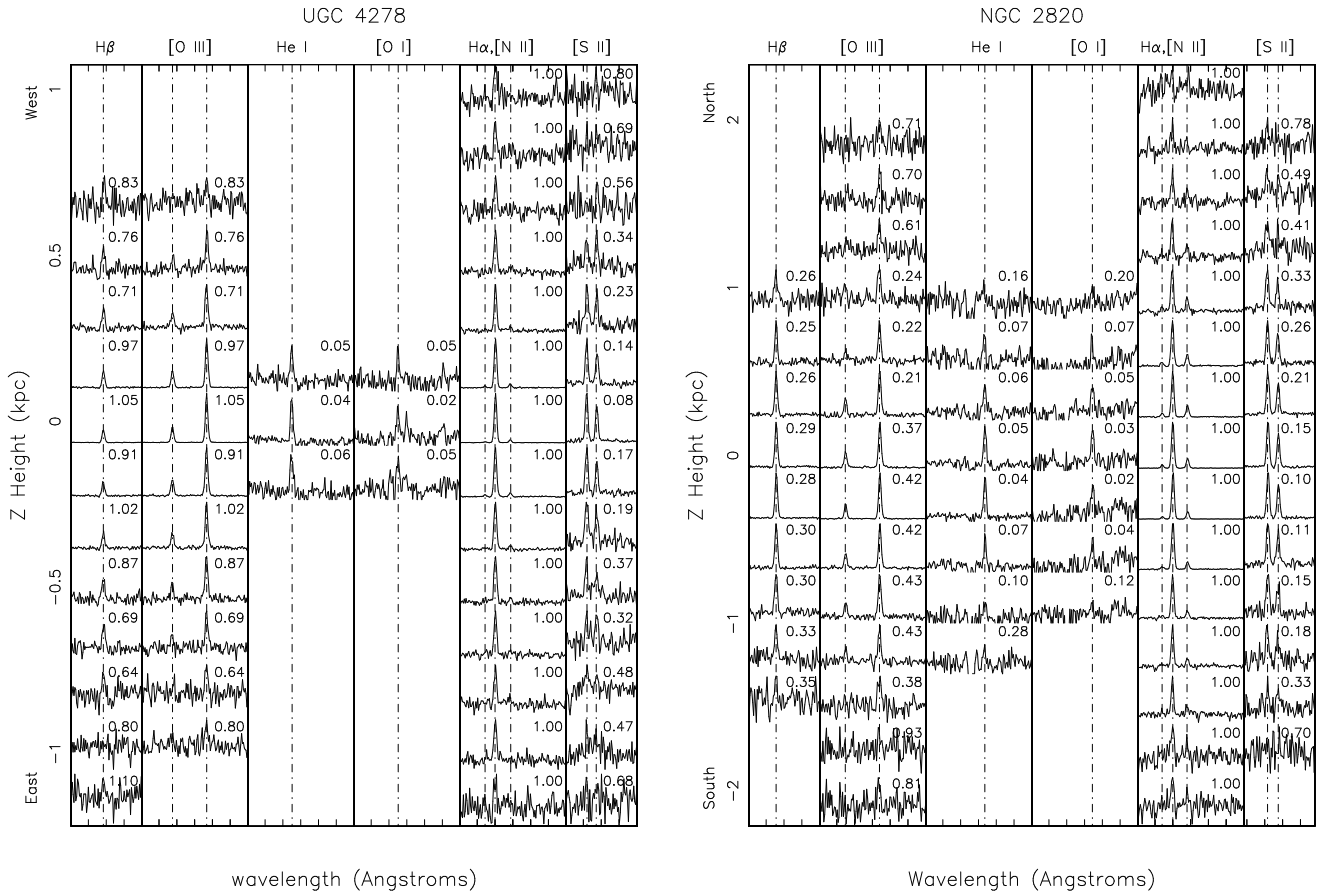


FIG. 2.— (Cont'd.)

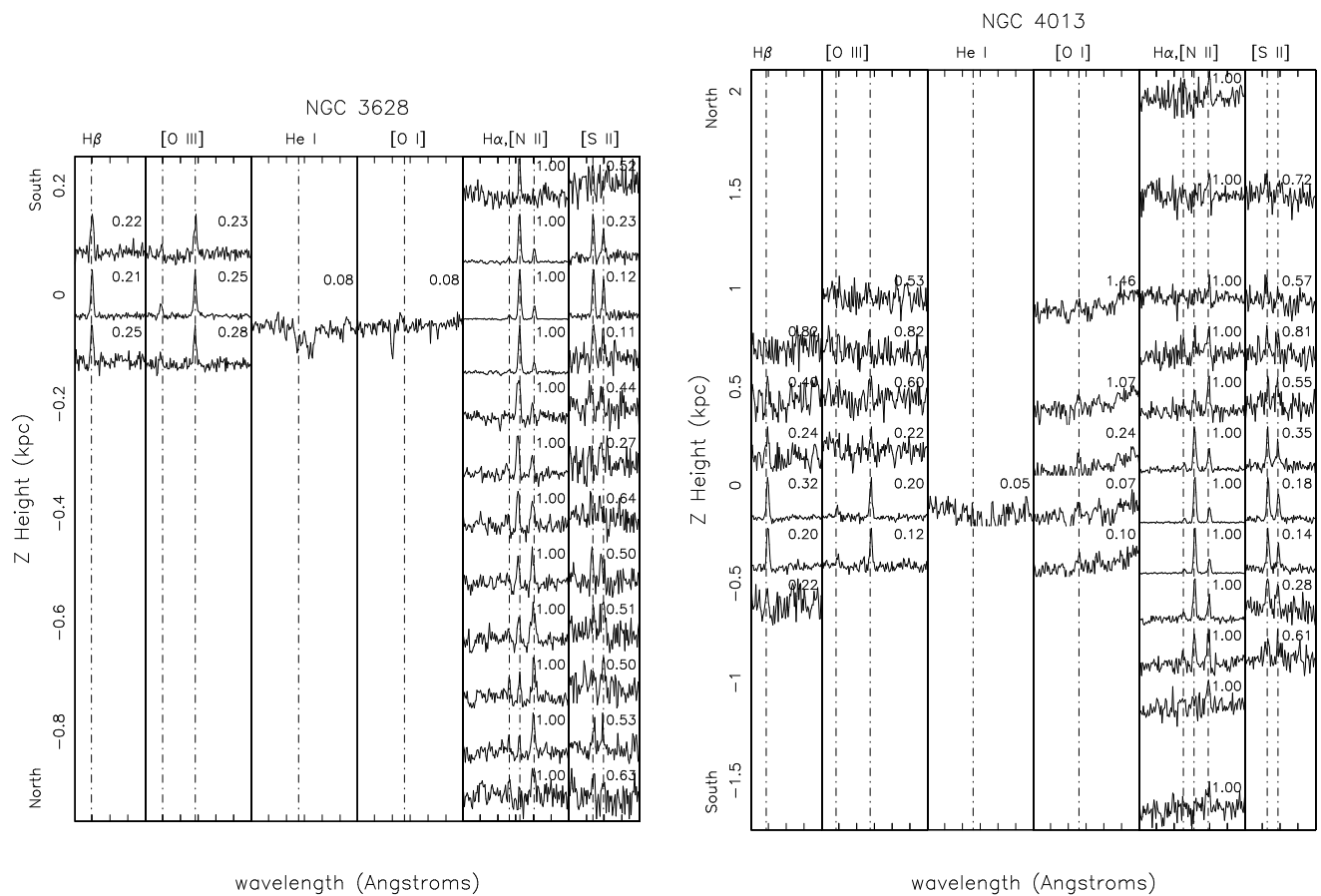


FIG. 2.— (Cont'd.)

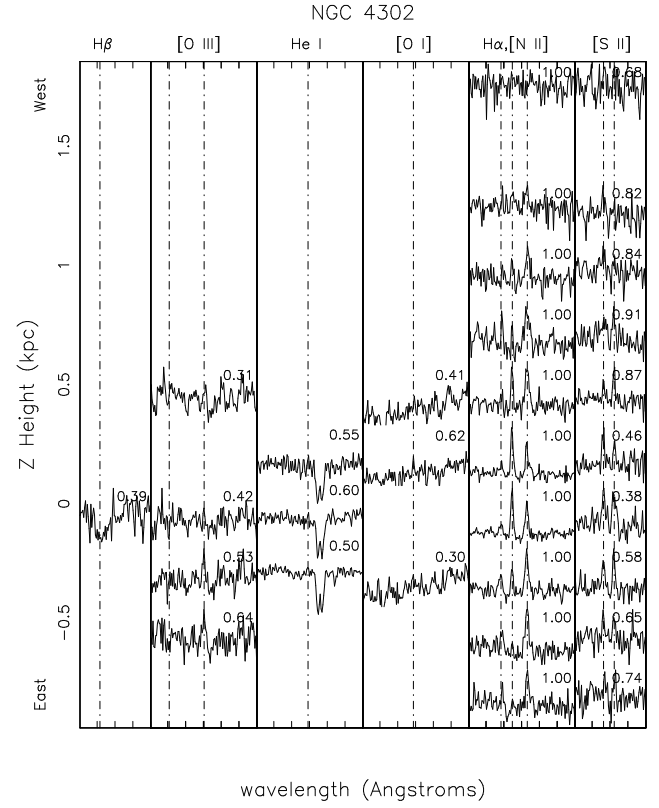
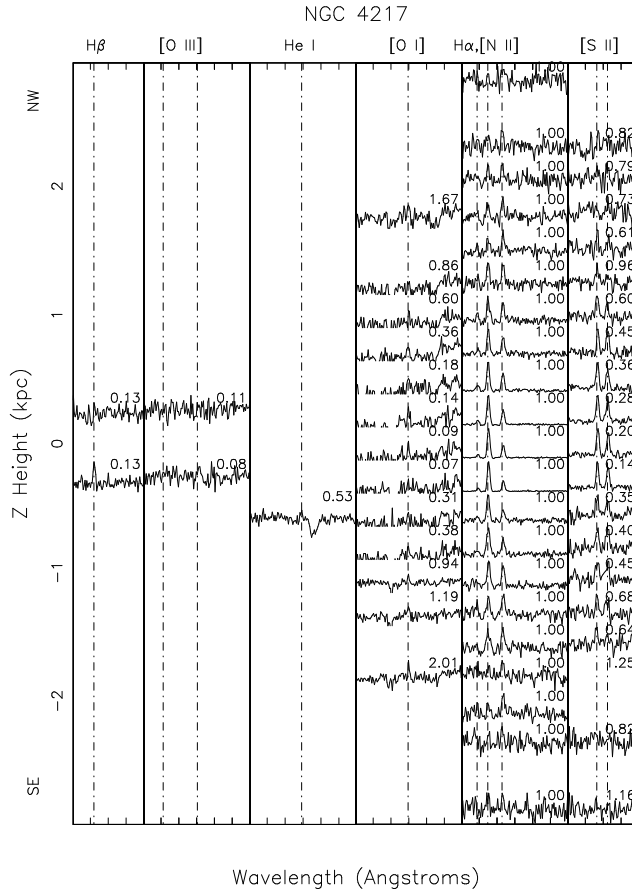


FIG. 2.— (Cont'd.)

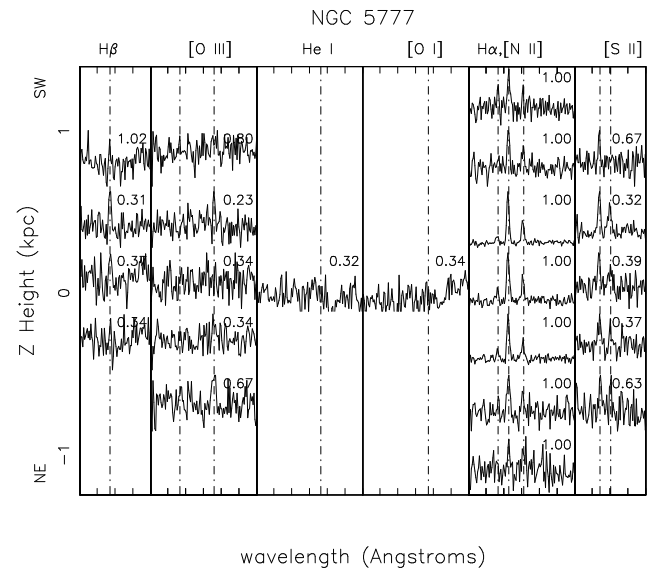
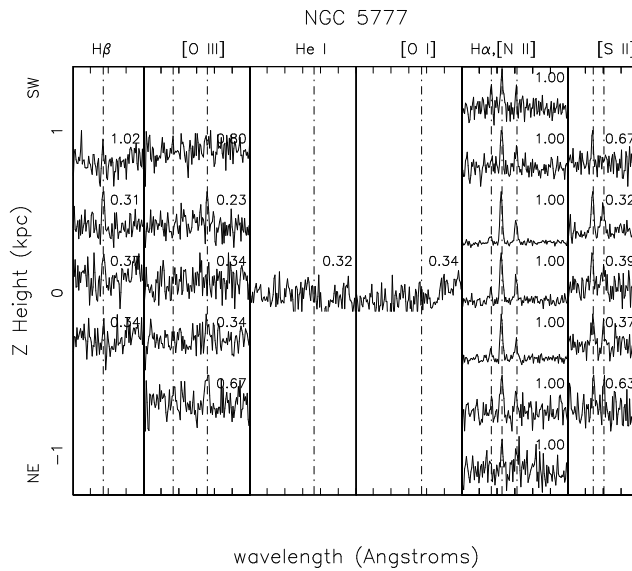


FIG. 2.— (Cont'd.)

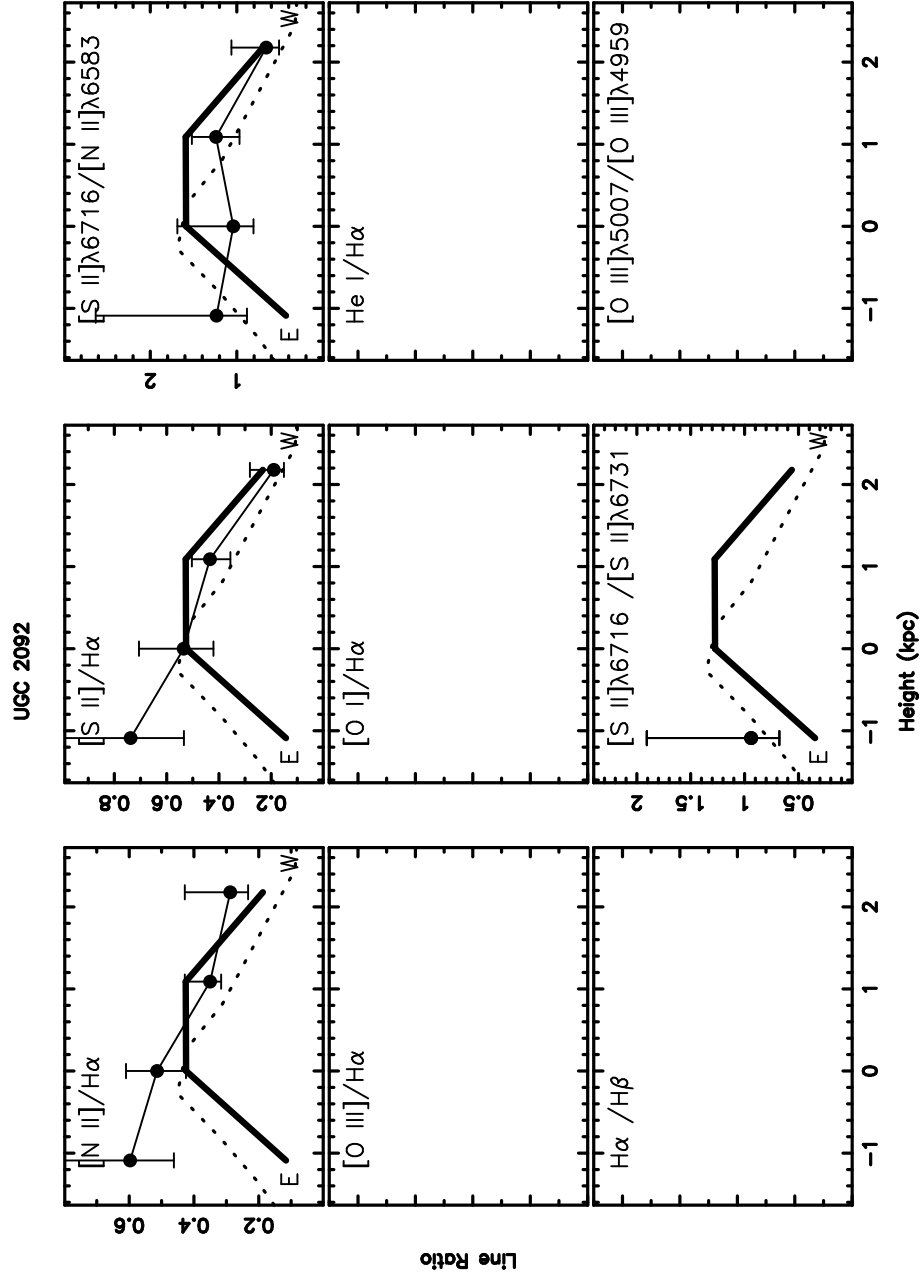


FIG. 3.—



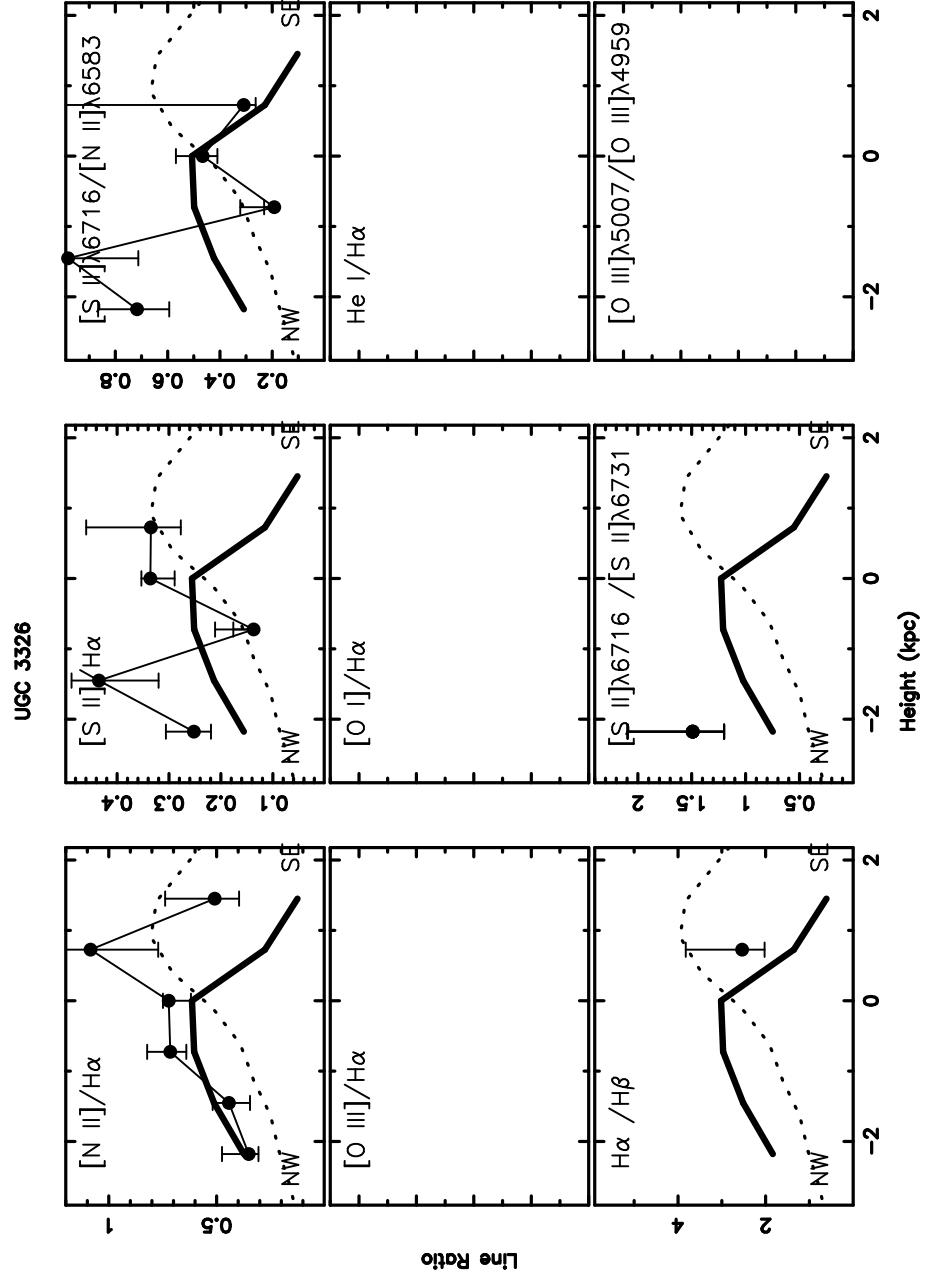


FIG. 3.— (Cont'd.)

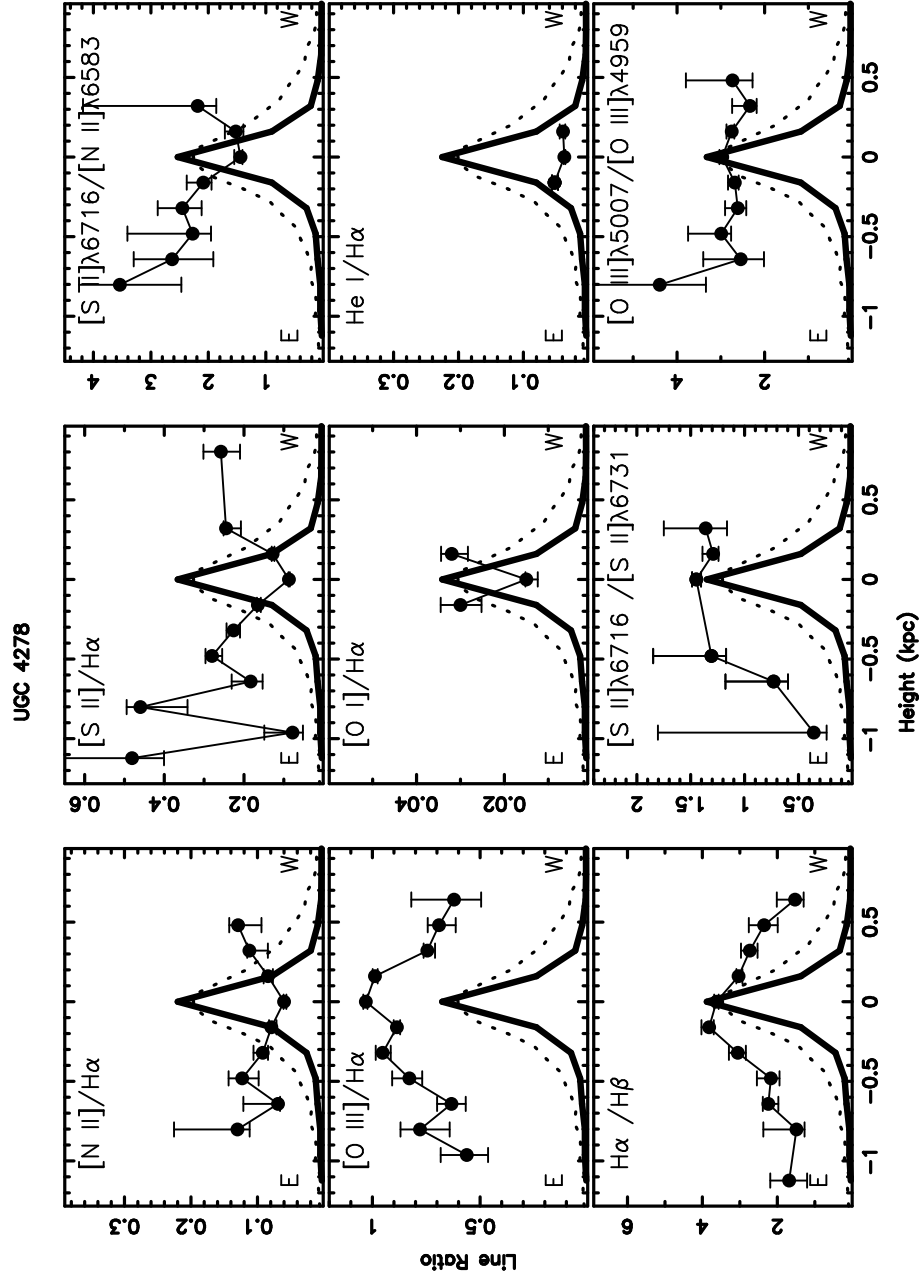


FIG. 3.— (Cont'd.)

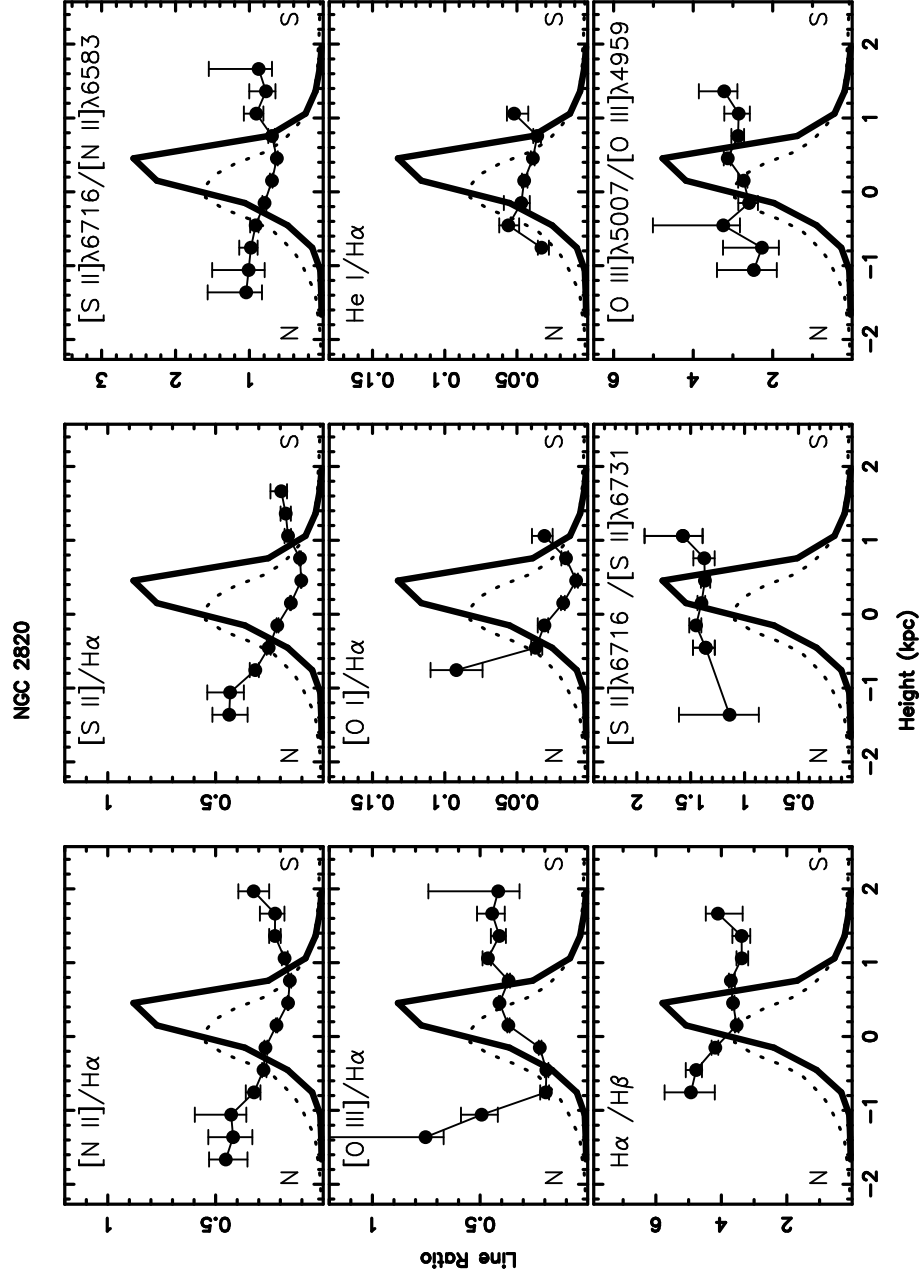


FIG. 3.— (Cont'd.)

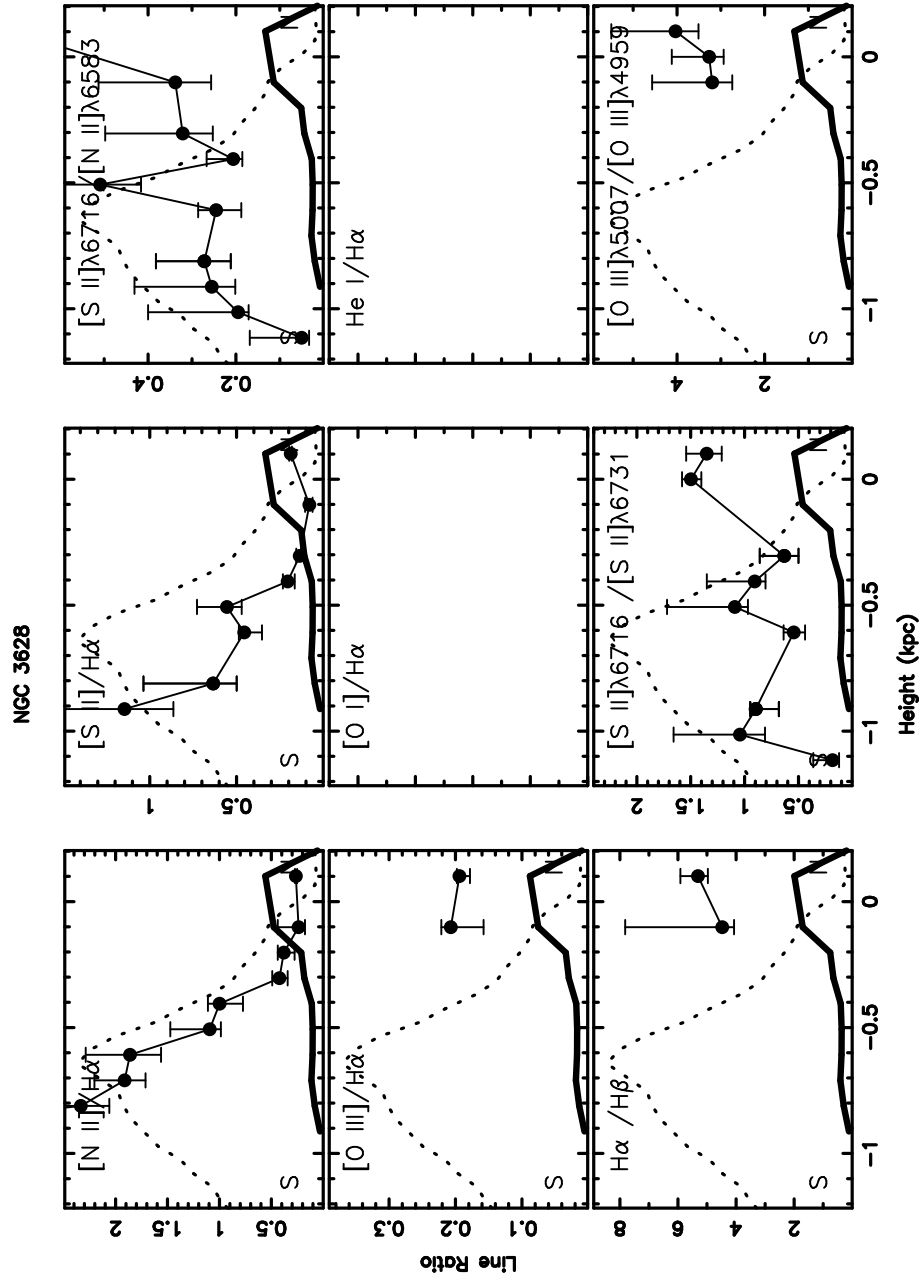


FIG. 3.— (Cont'd.)

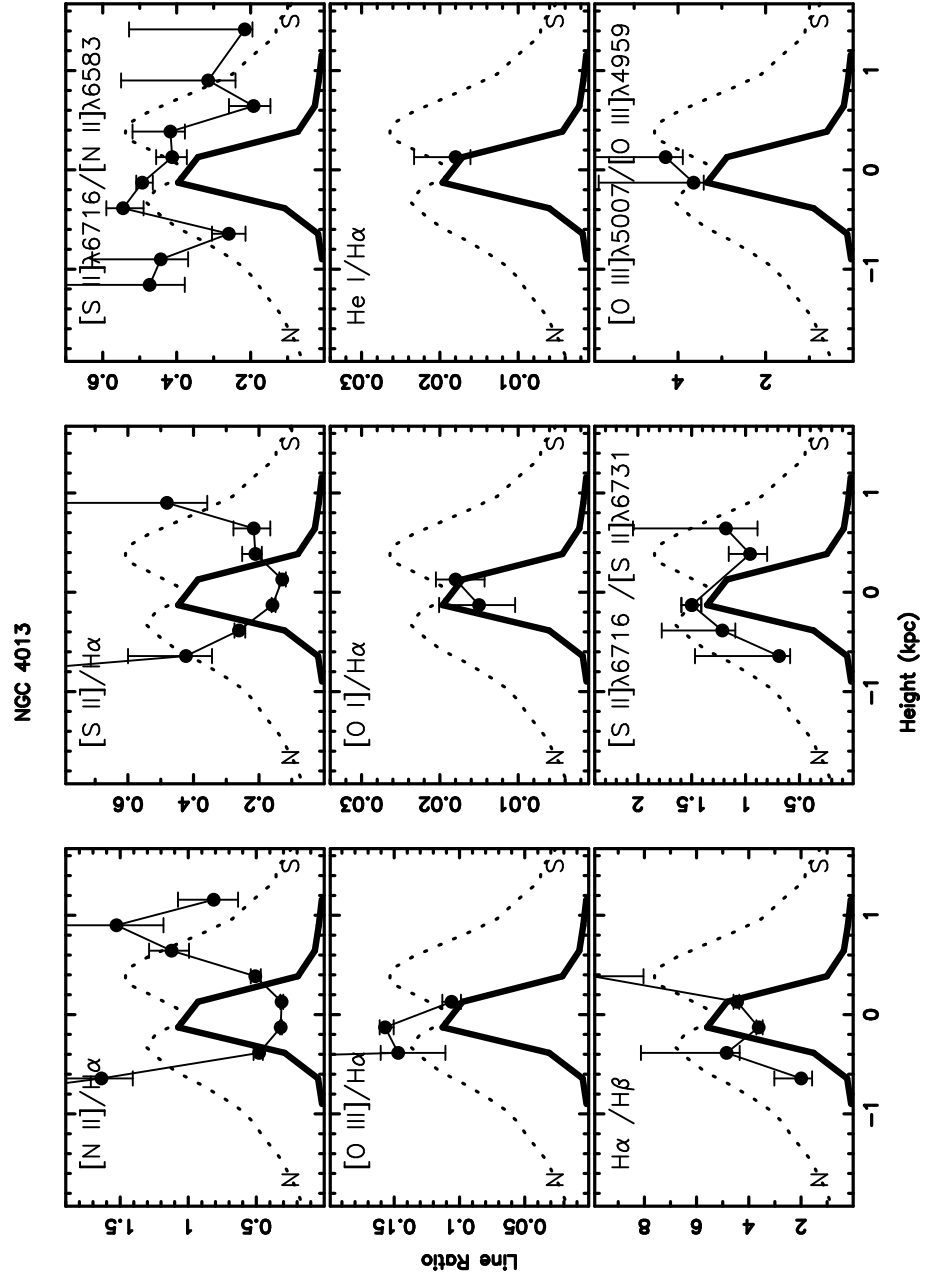


FIG. 3.— (Cont'd.)

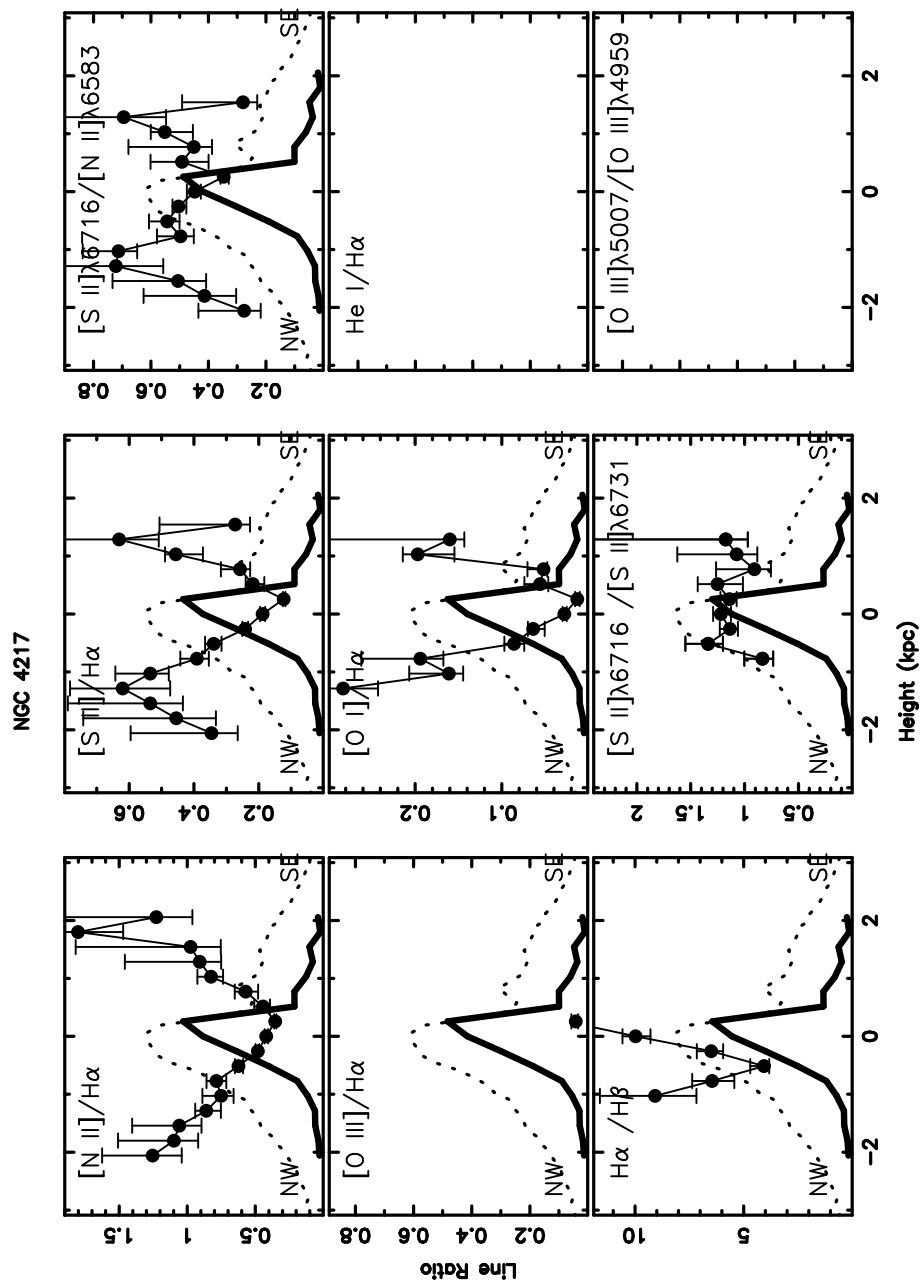


FIG. 3.— (Cont'd.)

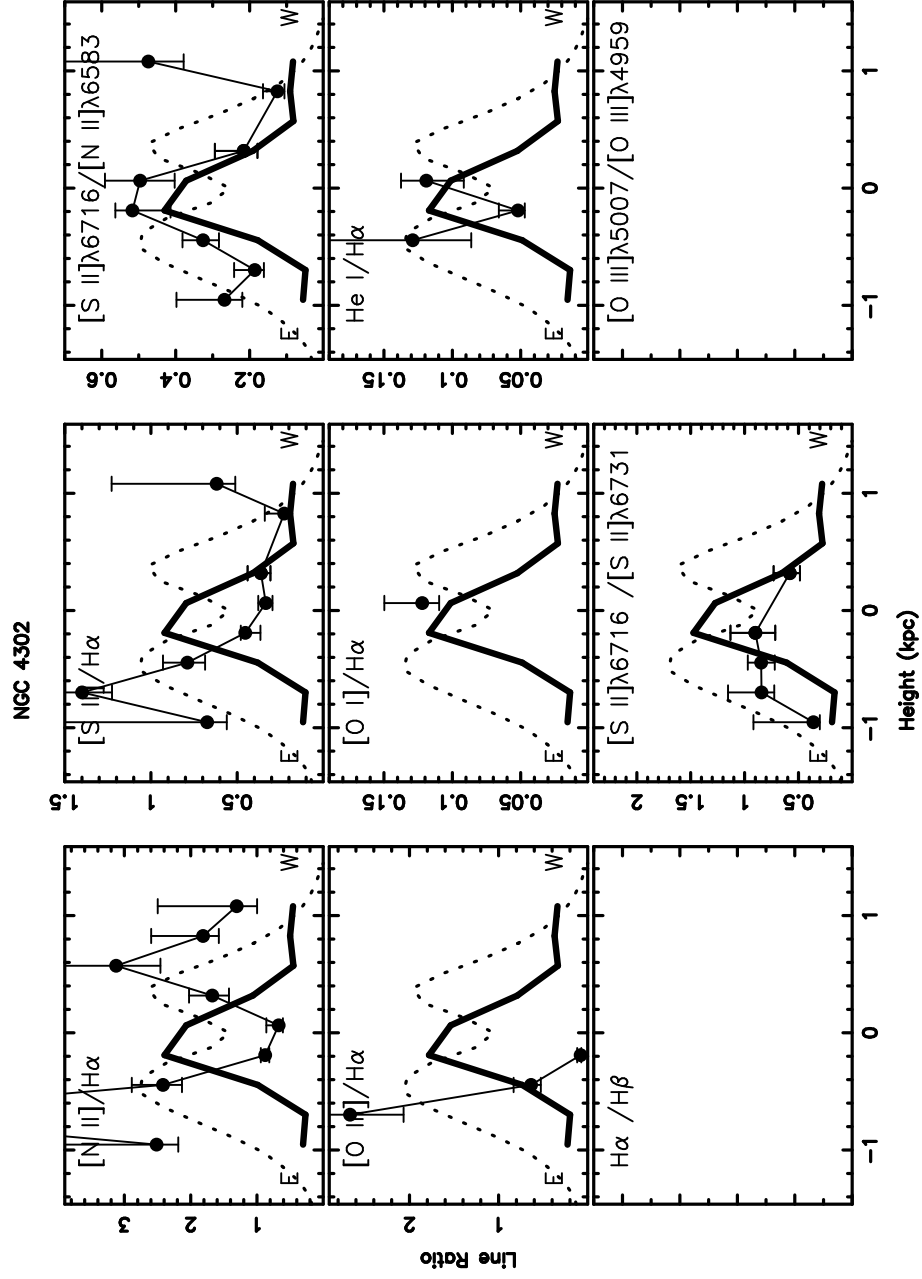


FIG. 3.— (Cont'd.)

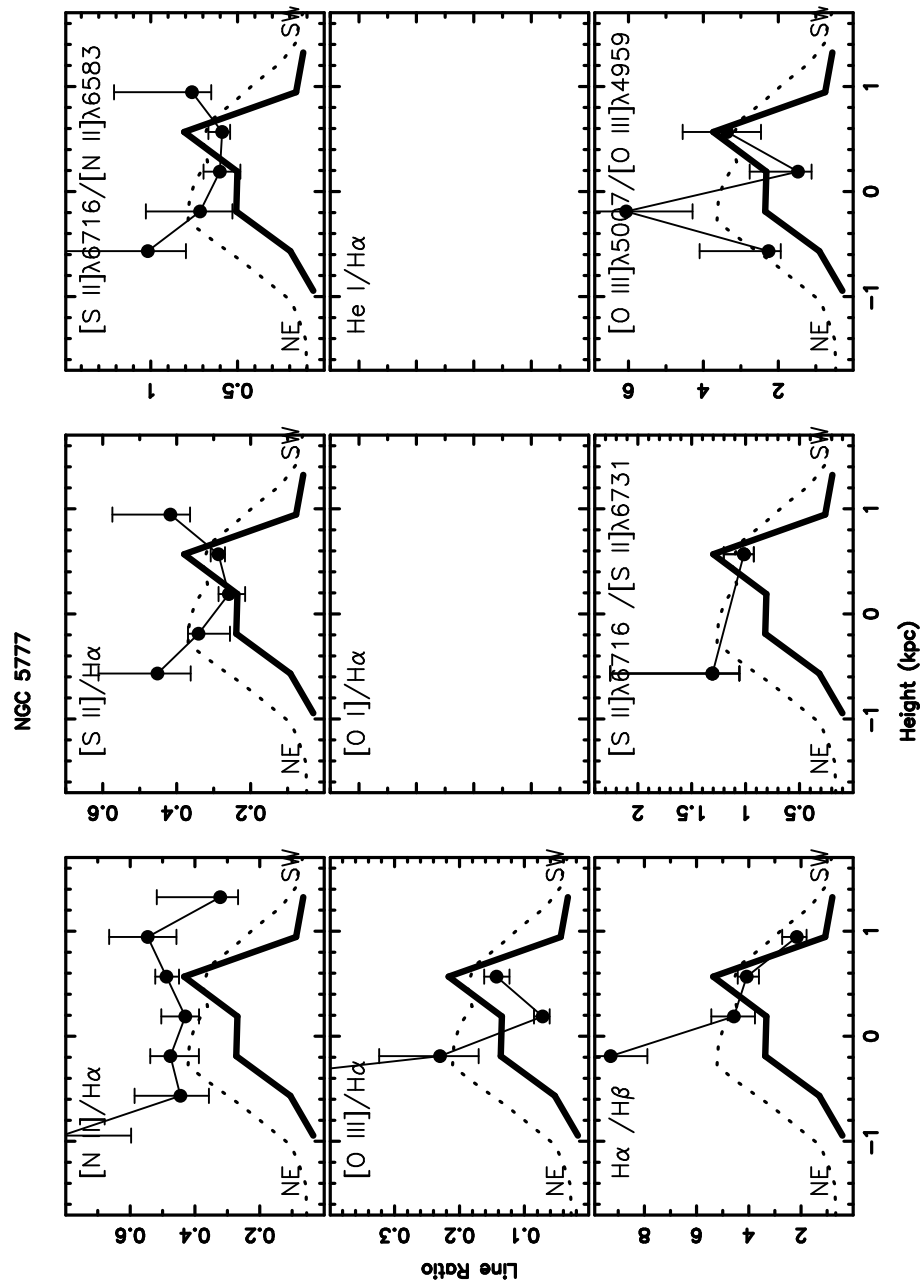


FIG. 3.— (Cont'd.)



TABLE 1  
SAMPLE

Galaxy	R.A. (J2000) <sup>a</sup> hh mm ss	Dec (J2000) <sup>a</sup> dd mm ss	D <sub>25</sub> <sup>a</sup> ( $''$ )	Disk P.A. <sup>a</sup> ( $^{\circ}$ )	Morphological Type <sup>a</sup>	Dist. <sup>b</sup> (Mpc)	Incl. <sup>b</sup> ( $^{\circ}$ )	Reference for Imaging Data
UGC 2092	02 36 30.0	+07 18 00	3.16	32	Scd	72 <sup>c</sup>	86 <sup>d</sup>	Pildis et al. 1994
UGC 3326	05 39 36.0	+77 18 00	3.55	84	Scd	48 <sup>c</sup>	90 <sup>d</sup>	Pildis et al. 1994
UGC 4278	08 13 59.0	+45 44 43	4.68	172	SB(s)d	10.6	90	Rand 1996
NGC 2820	09 21 47.1	+64 15 29	4.07	59	SB(s)c	20.0 <sup>c</sup>	90	Paper I
NGC 3628	11 20 16.3	+13 35 22	14.79	104	Sb	6.7	87	Fabbiano et al. 1990
NGC 4013	11 58 31.7	+43 56 48	5.25	66	Sb	17	90 <sup>d</sup>	Rand 1996, Paper I
NGC 4217	12 15 50.9	+47 05 32	5.25	50	Sb	17	86 <sup>d</sup>	Rand 1996
NGC 4302	12 21 42.5	+14 36 05	5.50	178	Sc	16.8	90 <sup>d</sup>	Rand 1996
NGC 5777	14 51 18.3	+58 58 35	3.09	144	Sb	25 <sup>c</sup>	83 <sup>d</sup>	Pildis et al. 1994

<sup>a</sup>Values taken from de Vaucouleurs et al. 1991.

<sup>b</sup>Values taken from Tully 1988 unless otherwise noted.

<sup>c</sup>References for distances: UGC 2092, UGC 3326, & NGC 5777 (Pildis et al. 1994), NGC 2820 (Hummel & van der Hulst 1989).

<sup>d</sup>References for inclinations: UGC 2092 & UGC 3326 (Guthrie 1992), NGC 4013 (Bottema 1995), NGC 4217 & NGC 4302 (Rand 1996), NGC 5777 (Guthrie 1992).

TABLE 2  
OBSERVING LOGS

Galaxy	Total Exposure Time	Number of Exposures	Slit P.A. ( $^{\circ}$ )	Distance from Nucleus
UGC 2092	5.75 hours	9	122	20''NE
UGC 3326	4.5 hours	7	107	16''SW
UGC 4278	5.0 hours	8	83	0''
NGC 2820	5.0 hours	7	139	19''NE
NGC 3628	3.75 hours	5	210	20''W
NGC 4013	4.5 hours	6	155	40''NE
NGC 4217	4.5 hours	6	144	50''SW
NGC 4302	4.5 hours	6	88	0''
NGC 5777	4.5 hours	6	54	50''SE

TABLE 3  
REDDENING FACTORS FOR IMPORTANT LINE RATIOS IF  $A_V = 1$

Line Ratio	Reddening
[N II] $\lambda 6583/H\alpha$	1.004
[S II] $\lambda 6716/H\alpha$	1.022
[O I] $\lambda 6300/H\alpha$	0.963
He I $\lambda 5876/H\alpha$	0.898
[O III] $\lambda 5007/H\alpha$	0.751
$H\alpha/H\beta$	1.381
[S II] $\lambda 6716/[N II] \lambda 6583$	1.021
[S II] $\lambda 6716/[S II] \lambda 6731$	0.998
[O III] $\lambda 5007/[O III] \lambda 4959$	1.012

This figure "f1a.jpg" is available in "jpg" format from:

<http://arxiv.org/ps/astro-ph/0304471v1>

This figure "f1b.jpg" is available in "jpg" format from:

<http://arxiv.org/ps/astro-ph/0304471v1>

This figure "f1c.jpg" is available in "jpg" format from:

<http://arxiv.org/ps/astro-ph/0304471v1>

This figure "f4a.jpg" is available in "jpg" format from:

<http://arxiv.org/ps/astro-ph/0304471v1>

This figure "f4b.jpg" is available in "jpg" format from:

<http://arxiv.org/ps/astro-ph/0304471v1>

This figure "f4c.jpg" is available in "jpg" format from:

<http://arxiv.org/ps/astro-ph/0304471v1>

This figure "f4d.jpg" is available in "jpg" format from:

<http://arxiv.org/ps/astro-ph/0304471v1>



This figure "f4e.jpg" is available in "jpg" format from:

<http://arxiv.org/ps/astro-ph/0304471v1>

This figure "f5a.jpg" is available in "jpg" format from:

<http://arxiv.org/ps/astro-ph/0304471v1>

This figure "f5b.jpg" is available in "jpg" format from:

<http://arxiv.org/ps/astro-ph/0304471v1>

This figure "f5c.jpg" is available in "jpg" format from:

<http://arxiv.org/ps/astro-ph/0304471v1>

This figure "f5d.jpg" is available in "jpg" format from:

<http://arxiv.org/ps/astro-ph/0304471v1>

This figure "f5e.jpg" is available in "jpg" format from:

<http://arxiv.org/ps/astro-ph/0304471v1>

This figure "f5f.jpg" is available in "jpg" format from:

<http://arxiv.org/ps/astro-ph/0304471v1>

This figure "f5g.jpg" is available in "jpg" format from:

<http://arxiv.org/ps/astro-ph/0304471v1>



This figure "f5h.jpg" is available in "jpg" format from:

<http://arxiv.org/ps/astro-ph/0304471v1>

This figure "f5i.jpg" is available in "jpg" format from:

<http://arxiv.org/ps/astro-ph/0304471v1>

This figure "f6a.jpg" is available in "jpg" format from:

<http://arxiv.org/ps/astro-ph/0304471v1>

This figure "f6b.jpg" is available in "jpg" format from:

<http://arxiv.org/ps/astro-ph/0304471v1>

This figure "f6c.jpg" is available in "jpg" format from:

<http://arxiv.org/ps/astro-ph/0304471v1>

This figure "f6d.jpg" is available in "jpg" format from:

<http://arxiv.org/ps/astro-ph/0304471v1>

This figure "f6e.jpg" is available in "jpg" format from:

<http://arxiv.org/ps/astro-ph/0304471v1>

This figure "f6f.jpg" is available in "jpg" format from:

<http://arxiv.org/ps/astro-ph/0304471v1>



This figure "f6g.jpg" is available in "jpg" format from:

<http://arxiv.org/ps/astro-ph/0304471v1>

This figure "f6h.jpg" is available in "jpg" format from:

<http://arxiv.org/ps/astro-ph/0304471v1>

This figure "f6i.jpg" is available in "jpg" format from:

<http://arxiv.org/ps/astro-ph/0304471v1>